Remote Sensing of Environment 333 (2026) 115122

Contents lists available at ScienceDirect

Remote Sensing of Environment

journal homepage: www.elsevier.com/locate/rse

Past, current and future solar radiation trends in Europe: Multi-source assessment of the role of clouds and aerosols

Leandro C. Segado-Moreno [a], José A. Ruiz-Arias [b,*], Juan Pedro Montávez [a], Juraj Betak [c]

[a] Department of Physics, University of Murcia, Murcia, Spain
[b] Department of Applied Physics I, University of Málaga, Málaga, Spain
[c] Solargis s.r.o., Bratislava, Slovakia

ARTICLE INFO

Edited by Menghua Wang

Keywords:
Solar radiation trends
Ground observations
Satellite-based model
Aerosol indirect effect
Climate projections

ABSTRACT

The increase of surface solar radiation (SSR) observed during the last decades in Europe has raised concerns for its implications for the climate system. Here, we evaluate the past and projected SSR trends in Europe from 1994 to 2054 based on a comprehensive set of ground site observations, five historical gridded datasets and a remarkable ensemble of 30 CMIP6 climate models with projections in four different forcing scenarios. Together, they provide a seamless unprecedented characterisation of the SSR trend in Europe across time and space. The regional SSR trend observed in the period 1994–2023 is 3.1 W/m^2/decade. All gridded datasets, except the ERA5 reanalysis, deviate from this value by ±0.3 W/m^2/decade, or less. Assuming that clouds and aerosols are the only boosters of the SSR trend, it is found that ≈20% of the trend is explained by aerosol direct effect (ADE). It is shown that the first aerosol indirect effect (AIE) alone cannot explain the SSR trend related to cloud changes, thus leaving a significant role for changes in cloud coverage. It is estimated that the total SSR trend is approximately explained in 1/5 by ADE, 2/5 by first AIE and 2/5 by cloud coverage changes. However, this fractions are likely affected by biases in aerosol optical depth. The results suggest that the CMIP6 ensemble overestimates (underestimates) the clear (cloudy) SSR trend during 1994–2014. The median SSR trend projected by the CMIP6 models is, on average, ≈85% smaller than the trend observed during 1994–2023 with small differences between forcings scenarios.

1. Introduction

Downward surface solar radiation (SSR) is the primary component of the global mean surface energy budget, supports life on Earth and drives the climate's fate (Wild et al., 2013). It is also the fundamental source of energy for solar thermal and photovoltaic technologies (Kalogirou, 2013). Although long-term variations of SSR are well known (Wild, 2012), and clouds and aerosols are known to be driving forces (Schilliger et al., 2024), their relative contributions are still unclear (Augustine and Dutton, 2013; Fang et al., 2020; Mateos et al., 2014; Ohmura, 2009; Padma Kumari and Goswami, 2010; Turnock et al., 2015; Wild et al., 2005).

Aerosols have a twofold impact on SSR. First, because they absorb and scatter solar radiation, but also because the absorption/scattering ratio alters the heating and cooling of the atmosphere and the clouds thermodynamics. The former is commonly referred to as aerosol direct effect (ADE) (Bellouin and Yu, 2022) while the latter is referred to as semidirect effect (Allen et al., 2019). Second, because they alter clouds processes and characteristics through mechanisms that are jointly referred to as aerosol indirect effect (AIE) (Lohmann and Feichter, 2005; Rosenfeld et al., 2014), most notably aerosol particles acting as cloud condensation nuclei (CCN) and ice nuclei. In particular, an increase in the number of CCN favours the formation of warm clouds with smaller and more numerous drops, contributing to the enhancement of cloud albedo (Twomey, or first, indirect effect; Twomey, 1977), lowering of precipitation efficiency and increase of cloud lifetime (Albrecht, or second, indirect effect; Albrecht, 1989).

In parallel, the rise of temperatures by global warming is also known to decrease cloud fraction (CF) (Goessling et al., 2025; Schneider et al., 2019), and thus having an impact on SSR. The reduction of CF with temperature is an intricate process (Luo et al., 2024), however, quantified by some studies. For example, McCoy et al. (2017) used satellite observations and reanalysis data to perform a regression analysis between sea surface temperature and low cloud cover. In a scenario with 0.2 K increase of estimated inversion strength and 1 K increase of sea surface temperature the low cloud cover decreased by 0.005–0.027. Lu et al. (2023) used retrievals of the Cloud-Aerosol Lidar

* Corresponding author.
E-mail address: jararias@uma.es (J.A. Ruiz-Arias).

https://doi.org/10.1016/j.rse.2025.115122
Received 22 January 2025; Received in revised form 26 October 2025; Accepted 3 November 2025
Available online 7 November 2025

with Orthogonal Polarisation (CALIOP) onboard the Cloud-Aerosol Lidar and Infrared Pathfinder Satellite Observation (CALIPSO) to derive a relationship between CF and cloud base temperature (CBT). Fig. 3a in that work shows that, for CBT>10 °C, the CF-CBT rate is ≈ −0.015/°C. Mendoza et al. (2021) developed a semi-empirical linear parameterisation according to which the rate of change of CF with surface air temperature is −0.015/°C if relative humidity is conserved and −0.076/°C otherwise.

Overall, the relative importance of ADE, AIE and global warming in the SSR trend is not yet fully understood, which is a source of concern due to the relevance of SSR for the global climate and global warming (Loeb et al., 2025), but also for strategic deployment of solar energy, as the magnitude and robustness of SSR trends can affect the long-term profitability of solar energy projects, thus influencing how solar resources are best exploited in the long run (Jerez et al., 2015; Wild et al., 2015).

Ground-based observations are considered the most reliable data source for SSR monitoring (Wild et al., 2017). However, the availability of research-class radiometric stations operated for multidecadal periods is scarce. Generally, they are present only in regions that have provided a long-term financial and technical support throughout time, and even there, they typically cover only a minuscule fraction of the territory. In addition, both proper maintenance protocols and stringent quality assurance algorithms, which prevent data degradation due to issues in radiometric sensors (e.g., originating from adverse environmental conditions, soiling, levelling problems, ageing, miscalibration, or sensor replacements), are difficult and expensive to apply regularly, typically resulting in biases and data artefacts that are especially harmful for the evaluation of multidecadal trends (Gilgen and Ohmura, 1999; Sanchez-Lorenzo et al., 2013; Urraca et al., 2024). The main limitation of ground-based data though is their spatial sparsity.

Satellite-based SSR datasets are surfacing to fill this gap (Pfeifroth et al., 2018; Pinker et al., 2005; Sanchez-Lorenzo et al., 2017; Schilliger et al., 2024). Recently, Urraca et al. (2024) presented an evaluation of four satellite-based SSR datasets in the 20-year period from 2001 to 2020 in Europe, where three of them, namely, the Climate Monitoring Satellite Application Facility (CM-SAF) SurfAce Radiation DAtaset Heliosat version 3 (SARAH-3; Pfeifroth et al., 2024), the CM-SAF cLoud, Albedo and surface RAdiation dataset from AVHRR data - Edition 3 (CLARA-A3; Karlsson et al., 2023b) and the National Aeronautics and Space Administration (NASA) Clouds and the Earth's Radiant Energy System Energy Balanced and Filled Edition 4.2.1 (CERES-EBAF Ed4.2.1; Kato et al., 2018), provided consistent decadal SSR trends (3.1 W/m^2, 3.3 W/m^2 and 3.1 W/m^2, respectively) compared to their observational counterpart on the ground surface (2.9 W/m^2). The benchmark analysis also included the European Centre for Medium-range Weather Forecast (ECMWF) Reanalysis version 5 (ERA5) atmospheric reanalysis (Hersbach et al., 2020), which largely underestimated (1.7 W/m^2/decade) the observed trend.

On a monthly time scale, the standard uncertainty of satellite-based SSR data sets is in the range 6–8 W/m^2 (or, ≈4%–6%), as it will be shown in Section 4.1, comparable to that of radiometric ground sensors (≈5%; Gilgen and Ohmura, 1999), which explains the consistent results found in the evaluation of the trend in SSR from satellite-based SSR data. Nevertheless, they usually rely on observations from a single spaceborne spectroradiometer that covers continental-scale areas, and thus any issue with the spectroradiometer or with the observed data stream, expected or not, spreads over the entire area (e.g., replacement of the spectroradiometer or sensor drift issues). Consequently, when assessing SSR trends derived from satellite-based datasets, a prior examination of their temporal stability is recommended to address and rectify potential inhomogeneities within the data. To that aim, ground-based observations are instrumental, provided that they are aggregated over all sites across the region to counterbalance station-wise errors, since errors are typically independent among different sites.

An inherent limitation of ground- and satellite-based SSR datasets is however that they are only available for the past, while numerical weather prediction (NWP) models can reconstruct the past and predict the future. When used to evaluate past SSR trends, however, NWP models have been found to largely underestimate the observed trends even using the most advanced NWP datasets, such as ERA5, as noted above (Urraca et al., 2024), or as reported worldwide by Loew et al. (2016) for 1979–2008 using models from the third and fifth phases of the Coupled Model Intercomparison Project (CMIP) of the World Climate Research Program (CMIP, 2025). Most climate projection studies have evaluated the multimodel ensemble means of successive CMIP phases. For example, Wild et al. (2015) analysed 39 CMIP phase 5 (CMIP5) models worldwide for the RPC8.5 scenario between 2006 and 2045, finding that they were only consistent with the sign of the SSR trend. They concluded that the projected changes in SSR "quantitatively may indicate the overall direction of changes to be expected in the longer run, while on shorter timescales (decadal variability), changes may well be larger", which shows the large uncertainty usually attained with projected SSR trends. Hence, for trend projections in the near future (≈1–2 decades ahead), predictions based on the latest ground- and satellite-based estimates might be alternative candidates to be used in benchmark analyses, for instance, assuming persistence of the trends, provided the main trend drivers evolve smoothly. More recently, He et al. (2022) evaluated 24 CMIP phase 6 (CMIP6) models using historical observations in China and their projections for 2050–2069, finding "systematic biases in historical SSR values due to model biases in cloud cover and clear-sky radiation, resulting in largely uncertain projections for future changes". The large uncertainty in the projections of the SSR trend is further exemplified by the results of Bartók et al. (2017), which used global CMIP5 models as initial and boundary conditions to run four regional climate models in Europe. The regional models surprisingly produced trends that were inconsistent with those of the global input models. However, despite the large uncertainties, climate models are the only approach to make multi-decadal projections of photovoltaic (PV) production, which have generally concluded that the expected impact of climate change is rather limited and unlikely to threaten solar PV (Jerez et al., 2015; Müller et al., 2019; Tobin et al., 2018).

This work addresses important research questions that ultimately pursue a holistic description of the SSR trend in Europe, during the past 30 years and for the next 30 years. To that end, it uses the Solargis-3.2 satellite-based gridded SSR dataset for the first time for the assessment of SSR trends. To do so, the dataset is first benchmarked against four well-known same-class gridded datasets and an atmospheric reanalysis product. Second, the five gridded datasets are used to characterise the spatial and temporal distribution of SSR trends in Europe in the period 1994–2023 and to discuss the role of clouds and aerosols. In parallel, an approach to estimate the contributions of ADE, first AIE and cloud coverage in the regional SSR trend is proposed. Finally, CMIP6 projections of the SSR trend for 2024–2054 are analysed in light of the findings for the period 1994–2023.

The datasets are presented in Section 2, while Section 3 describes the methods used to evaluate the trends of SSR, benchmark the gridded datasets and quantify the different contributions to the regional SSR trend. Section 4 presents the model benchmarking results, the spatial and temporal SSR characterisation, the roles of clouds on aerosols, and the analysis of projected trends. Section 5 discusses the conclusions.

2. Data

2.1. Ground-based SSR data

The ground-based SSR measurements are a subset of the Global Energy Balance Archive (GEBA; https://geba.ethz.ch/) in Europe for the period 1994–2019 that has been extended up to September 2023

with monthly SSR data from the World Radiation Data Centre (WRDC; http://wrdc.mgo.rssi.ru/).

GEBA is a worldwide multidecadal database of observed surface energy fluxes that is maintained by the Institute for Climate and Atmospheric Sciences at the ETH Zürich. It contains quality-checked monthly averages of various energy flux components, including SSR, in more than 2500 locations (Wild et al., 2017). Since GEBA was only available until the end of 2019 at the download time, the data at all selected locations were extended with monthly averages calculated from daily measurements available on the WRDC website at the GEBA radiometric locations. The combined GEBA/WRDC dataset spans nearly 30 years from 1994 to 2023, missing only the last three months (Sep.-Dec., 2023). In the following, the extended GEBA subset with WRDC data is simply referred to as the GEBA data set.

The particular selection of GEBA sites for this study was based on a comprehensive and iterative evaluation of multiple criteria. The initial stage considered all European sites, except those with latitude greater than 60° because the SSR estimates from geostationary satellites are not available there. Afterwards, the minimum distance between stations was limited to 50 km to avoid colinearity issues. To do so, the site with fewer valid month data was discarded. Then a minimum of 324 months (i.e., 27 equivalent years) was required for all sites. In so doing, significant temporal coverage is guaranteed in all locations. In fact, all sites have a temporal coverage of 90%, or greater, and about 90% of the sites have a coverage of 95%, or greater. Although the Sonnblick station, Austria, met these criteria, it was discarded because it is located in a mountainous area, creating spatial representativeness concerns when its observations are compared to gridded datasets such as those from satellite and climate models. In total, 62 GEBA sites were pre-selected.

All pre-selected ground sites were tested for inhomogeneities. To do this, three algorithms were considered: the standard normal homogeneity test (Alexandersson, 1986), the Pettitt test (Pettitt, 1979), and the Buishand test (Buishand, 1982). The latter in up to four different variations. All tests are included in the Python package pyHomogeneity (Hussain et al., 2023), which was used to perform the analysis from deseasonalized SSR time series with respect to long-term monthly averages. Almost at all sites, all or some of the tests detected one or more breakpoints in the continuity of the time series, which are potentially caused by measurement issues or actual atmospheric variability. However, only the former are true sources of inhomogeneity. To be more confident that atmospheric variability is not producing a false breakpoint, the changes at the breakpoints are required to be greater than a minimum threshold, under the assumption that changes caused by atmospheric variability are much smaller than when they are caused by measurement issues. To set the threshold value, the 5% uncertainty estimated for the GEBA observations (Gilgen and Ohmura, 1999), plus a safety margin of 2%, were considered, totalling a 7% threshold value. Furthermore, it was required that at least two of the three tests (in the case of the Buishand test, any of its four variations) detect a change point in the same month and year. According to these criteria, data from 15 sites were found inhomogeneous and therefore discarded from the posterior analyses (Figs. S1-S2). A visual inspection of the time series also recommended flagging the station at Madrid, Spain, even though it did not meet all the criteria to be considered inhomogeneous. In particular, this station's data showed a clear discontinuity on January 1996, detected only by the standard normal homogeneity test (Fig. S3). Table 1 lists the final 46 selected stations. Fig. S4 shows their locations on a map.

2.2. Gridded SSR datasets

Four different satellite-based gridded SSR datasets, namely Solargis-3.2, SARAH-3, CLARA-A3 and CEBAF-4.2.1 (condensed form of CERES-EBAF Ed4.2.1), and the ECMWF's ERA5 reanalysis product, are evaluated here. The Solargis-3.2 satellite-based dataset is thoroughly described because it is used for the first time in a long-term SSR trend study.

The Solargis-3.2 dataset belongs to the global Solargis database, which is built and operated by the homonym company (Šúri and Cebecauer, 2014; Solargis, 2025). The solar radiation database is generated with a proprietary model (Solargis v2.3.0) that combines satellite observations of cloud reflectance and NWP results based on the principles of the Heliosat method (Cano et al., 1986) and has been optimised to run on various geostationary satellites globally. The Heliosat method evaluates the all-sky solar irradiance at the surface by relating the reflectance observed from the satellite in the visible channel (indeed, a normalised parameter customarily referred to as cloud index or effective cloud albedo) and the clear-sky index (i.e., the ratio of all-sky solar irradiance at the surface to its clear sky counterpart) using an empirical formula specific to each model (see Perez et al., 2013, for examples of such a formula, including the Solargis model). Müller and Pfeifroth (2022) provides a detailed description of the general Heliosat method to which the interested reader is referred for further details. The clear-sky solar irradiance, which is needed to compute the clear-sky index, is evaluated with a radiative transfer model. The Solargis model uses Ineichen's (Ineichen, 2008, 2018), which will be replaced by SPARTA (Ruiz-Arias, 2023) in a forthcoming update. The Solargis model incorporates various additional enhancements that help improve cloud detection, such as over snow and other bright surfaces (using additional observations from infrared channels and NWP predictions of snow depth and air temperature, based on Dürr and Zelenka, 2009), and topographic corrections on complex terrain areas (Ruiz-Arias et al., 2010).

In particular, for the study region and the period under scrutiny, the Solargis SSR is evaluated from reflectance images gathered by the Meteosat Visible and Infrared Imager (MVIRI) aboard the Meteosat First Generation (MFG) satellite until December 2004 and, thereafter, by the Spinning Enhanced Visible and Infrared Imager (SEVIRI) aboard the Meteosat Second Generation (MSG) satellite. SSR is calculated at the native temporal resolutions of the MVIRI and SEVIRI imagers (i.e., every 30 min and 15 min, respectively) and provided in a 2 arc-min × 2 arc-min (roughly, 0.03° × 0.03°) longitude-latitude spatial grid. Aerosol extinction is included in the clear-sky solar irradiance calculations through daily averages of sub-hourly aerosol optical depth retrieved from the Modern-Era Retrospective Analysis for Research and Applications, version 2 (MERRA-2; Gelaro et al., 2017) until 2002, the Monitoring Atmospheric Composition and Climate II project (MACC-II; Inness et al., 2013) for 2003–2012, and the Copernicus Atmosphere Monitoring Service reanalysis (CAMS; Inness et al., 2019) thereafter. Likewise, absorptions by water vapour and ozone are included through daily averages of sub-hourly estimates retrieved from the Climate Forecast System Reanalysis (CFSR; NOAA NCEI, 2025b) until 2010 and the Global Forecast System (GFS; NOAA NCEI, 2025c) thereafter. All parameters are bilinearly interpolated and topographically downscaled, with proper scale heights, from their native resolutions to the satellite's spatial grid before being used in the clear-sky radiative transfer model. The Ineichen clear-sky model does not require surface albedo as it assumes an average value by design constraints. The new SPARTA model will use surface albedo from the NASA's Moderate-resolution Imaging Spectroradiometer (MODIS; Liang et al., 2002).

A column version of Solargis-3.2 is used to simulate SSR at the GEBA locations in addition to the simulation with the raster model. Although the column model is virtually identical to the raster model, they produce slightly different results (negligible for practical applications) just because, by design constraints, they perform slightly different spatial interpolations before and after the computation of SSR.

The Solargis SSR data has undergone multiple validations and benchmark exercises, always demonstrating outstanding performance. For example, Ineichen (2013) conducted a long-term comparison of SSR estimates from 6 satellite-based models against observations gathered at 18 radiometric sites that spread over Europe, North Africa and the Middle East, where Solargis was the best performing contender. The superiority of the Solargis dataset was reconfirmed later by another

Table 1
Selected GEBA sites. The Lat and Lon columns provide the station's latitude and longitude, respectively, in degrees, while the Elev column gives the site's elevation in metres above mean sea level.

ID	Station	Lon	Lat	Elev	ID	Station	Lon	Lat	Elev
1	Karlstad (SE)	13.47	59.37	46	24	Tours (FR)	0.72	47.45	108
2	Stockholm (SE)	17.95	59.35	24	25	Dijon (FR)	5.08	47.27	222
3	Norrkoepping (SE)	16.25	58.58	5	26	Nantes (FR)	−1.60	47.17	27
4	Visby (SE)	18.35	57.67	51	27	Bourges (FR)	2.37	47.07	161
5	Zoseni (LV)	25.90	57.14	188	28	Payerne (CH)	6.94	46.82	491
6	Lund (SE)	13.22	55.72	73	29	Klagenfurt (AT)	14.33	46.65	452
7	Malin Head,C. (IE)	−7.33	55.37	25	30	Odessa (UA)	30.63	46.48	64
8	Belmullet (IE)	−10.00	54.23	10	31	La Rochelle (FR)	−1.15	46.15	4
9	Hamburg UV-B (DE)	10.00	53.63	14	32	Limoges (FR)	1.28	45.82	282
10	Dublin Airport (IE)	−6.25	53.43	85	33	Clermont-Ferrand (FR)	3.17	45.78	332
11	Valentia (IE)	−10.25	51.93	30	34	Bordeaux (FR)	−0.70	44.83	49
12	Belsk (PL)	20.78	51.83	180	35	Montelimar (FR)	4.73	44.58	73
13	Ostrava-Poruba (CZ)	18.15	49.82	242	36	Embrun (FR)	6.50	44.57	871
14	Wuerzburg (DE)	9.97	49.77	275	37	Nice (FR)	7.20	43.65	4
15	Zakopane (PL)	19.97	49.28	857	38	Montpellier (FR)	3.97	43.58	5
16	Caen (FR)	−0.47	49.18	78	39	Marignane (FR)	5.22	43.43	4
17	Kucharovice (CZ)	16.08	48.88	334	40	La Coruna (ES)	−8.42	43.37	58
18	Brest (FR)	−4.42	48.45	99	41	Oviedo (ES)	−5.87	43.35	335
19	Weihenstephan (DE)	11.70	48.40	469	42	Perpignan (FR)	2.87	42.73	43
20	Wien-Hohe-Warte (AT)	16.37	48.25	202	43	Bastia (FR)	9.48	42.55	8
21	Rennes (FR)	−1.73	48.07	37	44	Ajaccio (FR)	8.80	41.92	4
22	Hohenpeissenberg (DE)	11.02	47.80	990	45	Valladolid (ES)	−4.77	41.65	734
23	Salzburg/Freisal (AT)	13.05	47.78	420	46	Murcia (ES)	−1.17	38.00	61

study now under the auspices of the World Bank Group Energy Sector Management Assistance Programme (World Bank Group, 2019). More recently, Solargis was ranked the best in an independent worldwide benchmark study that included the most prominent satellite-based and NWP-based models worldwide (Forstinger et al., 2023). The performance of the Solargis-3.2 dataset is further benchmarked here against the other satellite-based gridded datasets mentioned above and the ERA5 reanalysis product (Section 4.1). As all of them, except Solargis-3.2, have recently been benchmarked in Urraca et al. (2024), only a brief description is provided, and the interested reader is referred to that study for further details.

As Solargis-3.2, SARAH-3 (Pfeifroth et al., 2024) is based on the Heliosat method. It uses observations from MVIRI and SEVIRI but, unlike Solargis, uses optical properties from climatological aerosols. The dataset starts in 1983 and is provided only for the Meteosat grid area, in a 0.05°×0.05° longitude-latitude grid, with a time resolution of 30 min. In contrast to Solargis-3.2 and SARAH-3, CLARA-A3 (Karlsson et al., 2023b) uses observations from polar-orbiting satellites, which restricts its finest temporal resolution to 1 day. It operates globally with data available since 1979 on a 0.25°×0.25° longitude-latitude grid. As in SARAH-3, it uses climatological aerosol optical properties. The CEBAF-4.2.1 SSR is the result of a more sophisticated algorithm (Kato et al., 2018). It consists of a retrieval process that adjusts a previously computed monthly SSR dataset (Rutan et al., 2015) by forcing the top-of-atmosphere (TOA) irradiance computed with a radiative transfer model to match the homogenised CERES-EBAF TOA dataset (Loeb et al., 2018). It is a global dataset, available since March 2000, provided in a 1°×1° longitude-latitude grid with monthly time resolution. Lastly, ERA5 is the flagship ECMWF's reanalysis dataset, covering the global atmosphere since 1940 with hourly resolution in a 0.25°×0.25° longitude-latitude spatial grid. It uses climatological aerosols combined with anthropogenic sulphate emissions based on data from CMIP5 and stratospheric sulphate emissions from major volcanic eruptions (Hersbach et al., 2020).

2.3. CMIP6 data

CMIP6 encompasses simulations with independent climate models coordinated through multiple projects to pursue singular objectives (Eyring et al., 2016). In particular, the Scenario Model Intercomparison Project (ScenarioMIP) provides multimodel climate projections under eight alternative 21st century climate forcing pathways of future emissions and land use changes that constitute an important base of scientific evidence for the Intergovernmental Panel on Climate Change assessments (O'Neill et al., 2016). The forcing pathways are materialised through multiple Shared Socioeconomic Pathway (SSP) scenarios (Riahi et al., 2017). This study includes simulations of the four Tier 1 SSP scenarios (O'Neill et al., 2016), namely: SSP1-2.6 (sustainability scenario, or scenario 1, with a low radiative forcing of 2.6 W/m^2 by 2100), SSP2-4.5 (middle of the road scenario, or scenario 2, with a medium radiative forcing of 4.5 W/m^2 by 2100), SSP3-7.0 (regional rivalry scenario, or scenario 3, with high 7.0 W/m^2 radiative forcing by 2100), and SSP5-8.5 (fossil-fuelled development scenario, or scenario 5, with a high radiative forcing of 8.5 W/m^2 by 2100).

The ScenarioMIP projections considered in this study encompass 292 realisations from 30 CMIP6 climate models covering the period 2024–2055 for the four Tier 1 SSP scenarios (Table 2). More specifically, the ensemble of SSP1-2.6 realisations has 66 members, the SSP2-4.5 ensemble has 73 members, the SSP3-7.0 ensemble has 81 members and the SSP5-8.5 ensemble has 72 members. The selection of the models was based on: (1) the concurrent availability of three variables, namely, downward shortwave radiation flux at the surface (i.e., SSR, or *rsds* in the CMIP6 nomenclature), clear-sky downward shortwave radiation flux (i.e., SSR under an hypothetical cloudless sky, *rsdscs* in the CMIP6 nomenclature), and cloud fraction coverage (named *clt* in the CMIP6 nomenclature); and (2) the concurrent availability of model simulations in the Historical CMIP6 project (Eyring et al., 2016), which spans from 1850 to 2014 with models being forced with common data sets strongly based on observations. That is, the Historical CMIP6 project simulations do not run on scenario assumptions but on weather observations in the past. They serve here as a benchmark of the SSR trends obtained from the CMIP6 models for the period 1994–2014. This benchmark is deemed crucial for a proper performance assessment of the projected SSR trends in the period 2024–2055. The Historical CMIP6 ensemble considered here includes 113 members.

All CMIP6 data are retrieved from the Earth System Grid Federation nodes (Petrie et al., 2021).

2.4. Ancillary datasets

To explore the role of clouds and aerosols, the spatially-distributed SSR trends are compared with anthropogenic emissions, aerosol mass

Table 2
Description of the selected CMIP6 models. Further information for each model is provided in https://doi.org/10.22033/ESGF/CMIP6. <id>, where <id> is provided in the column "Number id".

Model	Institution	Year	Resol. (km)	Atm. model	Aer. model	Number id
ACCESS-CM2	CSIRO-ARCCSS	2019	250	MetUM-HadGEM3-GA7.1	UKCA-GLOMAP-mode	2281
ACCESS-ESM1-5	CSIRO	2019	250	HadGAM2	CLASSIC (v1.0)	2288
AWI-CM-1-1-MR	AWI	2018	100	ECHAM6.3.04p1		359
AWI-ESM-1-1-LR	AWI	2018	250	ECHAM6.3.04p1		9301
BCC-CSM2-MR	BCC	2017	100	BCC_AGCM3_MR		1725
BCC-ESM1	BCC	2017	250	BCC-AGCM3-LR		1734
CAMS-CSM1-0	CAMS	2016	100	ECHAM5-CAMS		1399
CESM2-WACCM	NCAR	2018	100	WACCM6	MAM4	10024
CIESM	THU	2017	100	CIESM-AM	MAM4	1352
CMCC-CM2-SR5	CMCC	2016	100	CAM5.3	MAM3	1362
CNRM-CM6-1-HR	CNRM-CERFACS	2017	100	Arpege 6.3	prescribed (TACTICv2)	1385
CanESM5	CCCma	2019	500	CanAM5	interactive	1303
EC-Earth3	EC-Earth-Consortium	2019	100	IFS cy36r4		181
FGOALS-g3	CAS	2017	250	GAMIL3		1783
GFDL-ESM4	NOAA-GFDL	2018	100	GFDL-AM4.1	interactive	1407
GISS-E2-2-H	NASA-GISS	2021	250	GISS-E2.2	none/OMA/TOMAS/MATRIX	15861
HadGEM3-GC31-MM	MOHC	2016	100	MetUM-HadGEM3-GA7.1	UKCA-GLOMAP-mode	420
INM-CM5-0	INM	2016	100	INM-AM5-0	INM-AER1	1423
IPSL-CM6A-LR	IPSL	2017	250	LMDZ		1534
KACE-1-0-G	NIMS-KMA	2018	250	MetUM-HadGEM3-GA7.1	UKCA-GLOMAP-mode	2241
MIROC6	MIROC	2017	250	CCSR AGCM	SPRINTARS6.0	881
MPI-ESM-1-2-HAM	HAMMOZ-Consortium	2017	250	ECHAM6.3	HAM2.3	1622
MPI-ESM1-2-HR	MPI-M DWD DKRZ	2017	100	ECHAM6.3	none/prescribed MACv2-SP	741
MPI-ESM1-2-LR	MPI-M AWI DKRZ DWD	2017	250	ECHAM6.3	none/prescribed MACv2-SP	742
MRI-ESM2-0	MRI	2017	100	MRI-AGCM3.5	MASINGAR mk2r4	621
NESM3	NUIST	2016	250	ECHAM v6.3		2021
NorESM2-LM	NCC	2017	250	CAM-OSLO	OsloAero	502
NorESM2-MM	NCC	2017	100	CAM-OSLO	OsloAero	506
TaiESM1	AS-RCEC	2018	100	TaiAM1	SNAP	9684
UKESM1-1-LL	MOHC NERC NIMS-KMA NIWA	2021	250	MetUM-HadGEM3-GA7.1	UKCA-GLOMAP-mode	16781

fractions, aerosol optical depth (AOD), CF and surface temperature data.

Anthropogenic emissions are collected from the Community Emissions Data System (CEDS), which provides gridded annual emissions of anthropogenic chemically reactive gases, carbonaceous aerosols and CO_2 for the period 1750–2014 (Hoesly et al., 2018). Specifically, combined emissions of sulphur dioxide (SO_2), nitrogen oxides (NOx), carbon monoxide (CO) and non-methane volatile organic compounds (NMVOC) aggregated at the country level are considered from the CEDS dataset version v_2025_03_18 (Hoesly et al., 2025).

Gridded monthly total AOD at 550 nm and aerosol mass fractions for the period 1994–2023 are gathered from NASA's MERRA-2 atmospheric reanalysis (Randles et al., 2017; GMAO, 2015). In addition, monthly ground observations of AOD from the Aerosol Robotic Network (AERONET; Giles et al., 2019) are used to evaluate the first AIE. As the availability of AERONET stations decreases rapidly over time, only the time period from 2004 to 2023 is covered. Prior to 2004, the number of stations becomes too small. The 45 selected stations are listed in Table S1.

Clouds are characterised with the CLARA-A3 gridded monthly total CF product (Karlsson et al., 2023a,b), which represents the fractional coverage of clouds within each grid cell (0.25°×0.25°).

Monthly spatially-averaged anomalies of surface air temperature (T_{as}) are retrieved from NOAA NCEI (2025a). They belong to the National Oceanic and Atmospheric Administration (NOAA) Global Surface Temperature Analysis, which combines sea surface and land temperature datasets as described in Vose et al. (2021).

3. Methods

3.1. Evaluation of trends

The SSR trends are calculated from deseasonalized SSR time series with respect to long-term monthly averages (also referred to as anomalies) to exclude the seasonal variability. The trend is determined with linear least squares regression and confidence intervals with a 95% confidence level. Statistical significance is further asserted with the Mann–Kendall test (Kendall and Gibbons, 1990), also with a confidence level of 95%.

Table 3
Analysis periods of the SSR trends.

Name	Start	End	Notes
Historical	1994-01	2014-12	CMIP6 Historical
Recent	2004-01	2023-09	Last 20 observational years
Observational	1994-01	2023-09	GEBA observations
Projected	2024-12	2054-12	CMIP6 projections

The trends are evaluated at every GEBA station and in every land cell of the gridded datasets. However, the local trends are more susceptible to include marginal trends (related to internal atmospheric variability) than region-wise trends, which are evaluated with data from multiple locations. Supporting this idea, Chtirkova et al. (2022) determined that there is just a 0.2% chance that the regional trend in Europe, derived from a combination of 56 locations (Sanchez-Lorenzo et al., 2015) during the brightening period, is solely caused by internal variability. Hence, in addition to the local trends, region-wise trends are also evaluated here from the mean of the anomalies at the 46 homogeneous GEBA locations and from the mean of the anomalies at all land cells of the gridded datasets. To improve the visualisation, the anomaly time series are displayed as 12-month running means.

3.2. Analysis periods

Chtirkova et al. (2022) suggested also a 23-year minimum threshold to evaluate SSR trends because, using data from Lindenberg (Germany) as a reference, determined that the SSR trend could not be fully compensated for by internal atmospheric variability. Therefore, the SSR trends are analysed for three different past time periods, equal to or longer than 20 years, and for one 30-yr projected period, as shown in Table 3.

In particular, one period spans the time interval with GEBA and gridded SSR data (thus named Observational period), while another focusses on the overlapping years of the Observational period and the CMIP6 Historical experiment (Eyring et al., 2016) (thus being named Historical period). The last 20 years of the Observational period are referred to as Recent period.

3.3. Benchmark of the SSR gridded datasets

The validation and benchmark of the SSR gridded datasets is performed at the 46 homogeneous GEBA stations based on the mean bias deviation (MBD) and the root mean square deviation (RMSD) (Gueymard, 2014). These two metrics are evaluated month by month for all sites combined (resulting in two time series of MBD and RMSD values, useful to assess the temporal stability of the models) and site by site for all the available data within the time period (resulting in as many MBD and RMSD values as ground sites, one for each ground site). In the latter case, the metrics are specifically referred to as site MBD (sMBD) and site RMSD (sRMSD) and two additional error scores are computed: the inter-quartile range (IQR), that is, the difference between the third and first quartiles of the sMBD and sRMSD values, and the interpercentile range 80 (IPR80), which is the difference between the percentiles 90 and 10.

3.4. Evaluation of the SSR trend by ADE

The Solargis-3.2 column model was run at the GEBA locations alternatively using daily AOD inputs (as done by the official Solargis-3.2 dataset) and a long-term monthly AOD climatology built from the daily AODs. As the AOD climatology does not contribute to the SSR trend, the differential trend between the two simulations is attributable to the extinction of SSR by aerosols and is hereafter referred to as ADE trend.

3.5. Evaluation of the SSR trend by first AIE

The first aerosol indirect effect (or Twomey effect), α, which accounts for the change of cloud albedo induced by aerosol particles, is defined in Feingold et al. (2003) as:

$$\alpha = -\frac{\partial \ln r_e}{\partial \ln \sigma_a} \tag{1}$$

where r_e is the effective radius of cloud droplets and σ_a is the aerosol optical depth. Feingold et al. (2003) pointed out that the maximum value of α is 0.33, while measurements yielded values in the range 0.02–0.16. Both liquid water path, L, and r_e determine the cloud optical depth, τ_c, as (Kokhanovsky, 2004):

$$\tau_c = \frac{3}{2}\frac{L}{\rho_w r_e} \tag{2}$$

where ρ_w is the water density. For a cloud with constant L, it follows that $\epsilon_{\tau_c} = \alpha\epsilon_{\sigma_a}$, where ϵ_x is the change of x relative to the mean of x.

The all-sky SSR, E_a, is evaluated from the cloud transmittance, T_c, and the clear-sky SSR, E_c, as $E_a = T_c E_c$, and, for a nonabsorbing cloud with asymmetry parameter g_c (Petty, 2006):

$$T_c = \frac{1}{1+(1-g_c)\tau_c}, \tag{3}$$

Therefore, the relative change of E_a by first AIE due to a relative change in σ_a is:

$$\epsilon_{E_a} = -\alpha\frac{(1-g_c)\tau_c}{1+(1-g_c)\tau_c}\epsilon_{\sigma_a} \tag{4}$$

As $g_c < 1$, increases of σ_a produce decreases of E_a, as expected. With typical parameter values (e.g., $\alpha = 0.1$, $g_c = 0.8$, $\tau_c = 10$ and $\sigma_a = 0.12$) a decrease of 0.01 in the magnitude of σ_a increases E_a by 0.5%.

3.6. Evaluation of the SSR trend by cloud coverage

The all-sky SSR can be evaluated in terms of cloud coverage, C, as:

$$E_a = CE_d + (1-C)E_c \tag{5}$$

where E_d is the cloudy-sky SSR. Taking the derivative with respect to C, the change of E_a can be written as $\Delta E_a = (E_a - E_c)\,\Delta C/C$, where ΔC is the change in C. The relative change of E_a in response to a relative change in C then is:

$$\epsilon_{E_a} = -\frac{1-K_c}{K_c}\epsilon_C \tag{6}$$

where $K_c = E_a/E_c$ is known as clear-sky index. On a monthly scale, $0 < E_a \le E_c$ and thus increases of C result in decreases of E_a and vice versa, as expected. More specifically, if K_c is equal to 0.5, a relative decrease of 1% in C would induce an increase of 1% in E_a. For clearer skies, the sensitivity of E_a to changes in C decreases, while it increases under cloudier periods.

Cloud coverage can change due to a multitude of processes and factors. Two of the most significant are the second AIE and air temperature. As the former is difficult to quantify, especially in a long-term context, the cloud coverage trend here is assumed to be related to a trend in air temperature. In particular, with constant relative humidity, the change in cloud coverage by a change in the air temperature of the troposphere, T_a, is (Mendoza et al., 2021):

$$\Delta C = -\frac{0.015}{^\circ\mathrm{C}}\Delta T_a \tag{7}$$

where ΔC and ΔT_a are the changes in C and T_a, respectively. From Eqs. (6)–(7), the relative change of E_a by a change in T_a is:

$$\epsilon_{E_a} = \frac{0.015}{^\circ\mathrm{C}}\frac{1-K_c}{K_c}\frac{\Delta T_a}{\bar{C}} \tag{8}$$

where $\bar{C}$ is the mean cloud coverage. This expression shows that increases of T_a produce increases of E_a (because C decreases), as expected. With typical values of cloud coverage ($\bar{C} = 0.6$) and clear-sky index ($K_c = 0.6$) a 0.5 °C increase in temperature increases E_a by 0.8%.

4. Results

4.1. Evaluation of the SSR gridded datasets

Fig. 1 shows the 12-month running means of monthly MBD and RMSD for the gridded datasets in the 46 homogeneous GEBA stations combined. The time-evolving biases of the datasets are disparate. While CEBAF-4.2.1 remains relatively unbiased and the bias of SARAH-3 stays roughly constant at ≈2%, ERA5 evidences a steady improvement with a reduction from ≈4% to less than 2%. In contrast, the biases of CLARA-A3 and Solargis-3.2 show varying regimes throughout time. The former has ≈1% bias prior 2005, then remains unbiased until 2015 when, again, the bias increases approaching 2%. The bias of Solargis-3.2 before 2005 stays between 1% and 2%, but vanishes thereafter. The reasons for that are discussed later.

The RMSD shows a steady reduction in all datasets. In general, ERA5 has the highest RMSD but also the highest improvement rate, clearly benefited by its large bias improvement mentioned above. Solargis-3.2 is the model with the lowest RMSD throughout the study period, closely followed by CLARA-A3 until 2015, when due to its increased bias, the RMSD starts to increase. Then, SARAH-3 and CEBAF-4.2.1 follow in increasing order of RMSD magnitude. Among the possible explanations for the small RMSD of Solargis-3.2 might be its high spatial and temporal resolutions and the use of daily aerosols.

Table 4 shows negligible mean sMBD for Solargis-3.2, CLARA-A3 and CEBAF-4.2.1, with Solargis-3.2 also having the lowest sMBD IQR and IPR80. Although SARAH-3 has the highest sMBD IQR, its sMBD

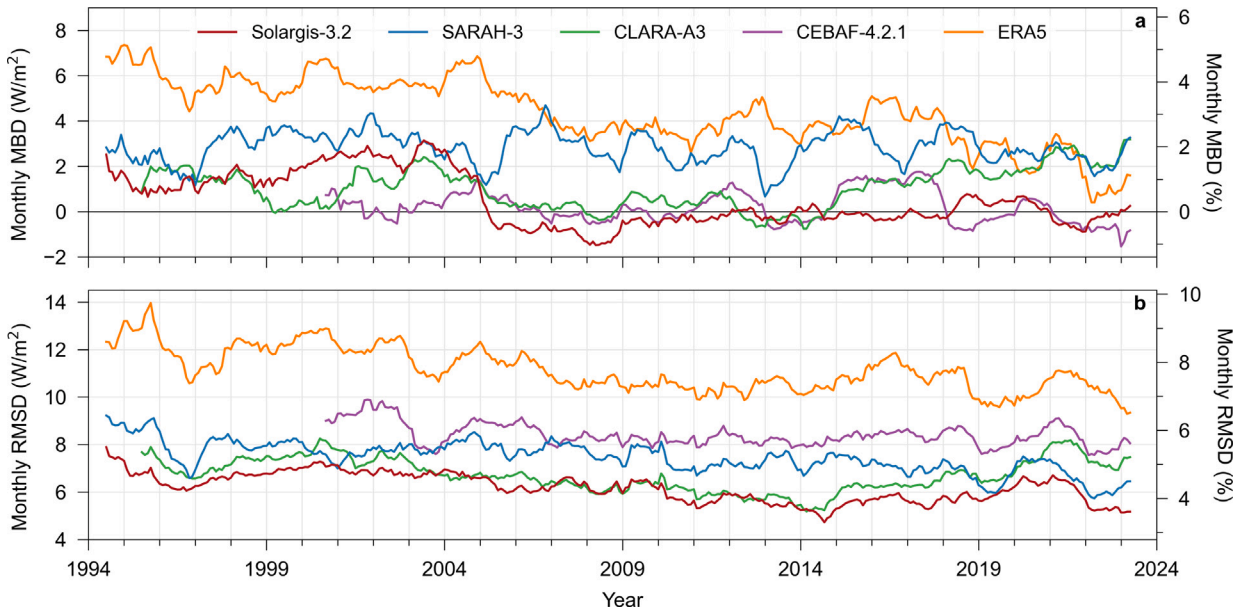

Fig. 1. 12-month running means of (a) monthly MBD and (b) monthly RMSD for all the SSR gridded datasets. The MBD and RMSD error metrics are evaluated over all homogeneous GEBA stations (Table 1). The percentage in the right axis is relative to the mean observed SSR in the combined GEBA stations during the Observational period.

Table 4
Ensemble statistics of the site MBD and site RMSD metrics (in W/m^2) for the Observational period (except for the CEBAF-4.2.1 dataset, which starts on March 2000). The calculations are performed over the homogeneous GEBA stations (Table 1).

Dataset	Site MBD				Site RMSD			
	Mean	Median	IQR	IPR80	Mean	Median	IQR	IPR80
Solargis-3.2	0.53	−0.06	3.01	6.05	6.39	6.17	1.68	2.94
SARAH-3	2.83	3.56	6.41	10.00	7.57	7.05	2.78	4.68
CLARA-A3	1.14	0.91	5.12	8.04	6.95	6.53	2.74	4.64
CEBAF-4.2.1	0.20	−0.08	5.18	12.17	8.57	7.58	4.07	10.25
ERA5	4.39	3.26	5.09	11.95	11.09	9.79	2.99	8.57

IPR80 is lower than those of CEBAF-4.2.1 and ERA5, meaning that the sMBD of these two reach more extreme values than SARAH-3. Likewise, Solargis-3.2 is the top performer with respect to sRMSD, providing the lowest values for all the sRMSD-related metrics. These results indicate that Solargis-3.2 is not only virtually unbiased, when computing bias sitewise, but is also the most precise dataset, since it produces the smallest IQR and IPR80 sRMSD metrics, therefore being the most robust dataset throughout the study region. The large dispersion of CEBAF-4.2.1 and ERA5 for both sMBD and sRMSD suggests problems in representing intra-regional variability. In the case of CEBAF-4.2.1, this is probably caused by its coarse spatial resolution. With ERA5, the cause might be an under-representation of some cloud types (Ruiz-Arias et al., 2016) and a misrepresentation of aerosols (Gao et al., 2025).

In general, a stable bias throughout time is crucial for a proper evaluation of the long-term trend. However, a low RMSD is required to ensure a spatially consistent dataset. In that regard, Solargis-3.2 is the best among the datasets considered here. However, it is handicapped for the evaluation of long-term trends by the 2005 MBD step shown in Fig. 1a, which is explained by the enhanced performance brought about by SEVIRI. The precise change point was evaluated from the difference between the average deseasonalized Solargis-3.2 SSR time series and observed SSR time series over all homogeneous GEBA stations. It yielded a change of 1.86 W/m^2, which was rectified by subtracting that amount from all cells in the satellite grid prior to November 2004. The resulting homogenised dataset is unbiased throughout the study period (Fig. 2), and is the one used to perform all the trend evaluations with the Solargis-3.2 dataset hereafter. The same approach was followed for the Solargis-3.2 column model. This homogenisation approach explicitly assumes that the spatial structure of the Solargis-3.2 error is uniform throughout the study region. However, mountainous areas present singular challenges for satellite-based SSR models that are related to complex topography (e.g., shadow casts by surrounding terrain), frequent and persistent snowed surfaces, and local fine-scale orographic clouds. Together, they compose an idiosyncratic error in mountainous areas for which the relative improvements enabled by SEVIRI are significantly greater than in other regions, thus making the wide-area homogenisation assumptions not valid there. For such a reason, mountainous areas are excluded here from trend evaluations in the Solargis-3.2 dataset before 2005.

4.2. Ground- and model-based SSR trends

Table 5 shows the regional SSR trends in the study region. When they are evaluated from the mean SSR anomaly across the 46 homogeneous GEBA locations (GEBA sites), the observed trend during the Recent period (3.0 W/m^2/decade) is greater than during the Historical period (2.7 W/m^2/decade), and both are smaller than the trend during the Observational period (3.1 W/m^2/decade, or 2.2%/decade, with respect to the mean observed SSR during the whole period). Only Solargis-3.2 and SARAH-3 are within a difference of ±0.2 W/m^2/decade with respect to the trend obtained from the GEBA observations for the three periods. CLARA-A3 clearly underestimates the trend observed in the GEBA stations during the Historical period while overestimates it during the Recent period. ERA5 always underestimates the observed trend by 50%, or more. These results are consistent with the MBD shown in Fig. 1 (e.g., the decreasing MBD of ERA5 explains its noticeable underestimate of the observed trend, while the fairly stable MBD of SARAH-3 favours a close estimate). They are also aligned with the trends recently reported by Urraca et al. (2024), considering the slightly different evaluation periods and GEBA locations.

When the regional SSR trend is instead evaluated from the average anomaly across all land grid cells of the modelled datasets (land areas), the trend value is generally lower than in the combined GEBA locations, suggesting that the spatial distribution of the GEBA locations would overestimate the actual regional SSR trend. In general, considering that

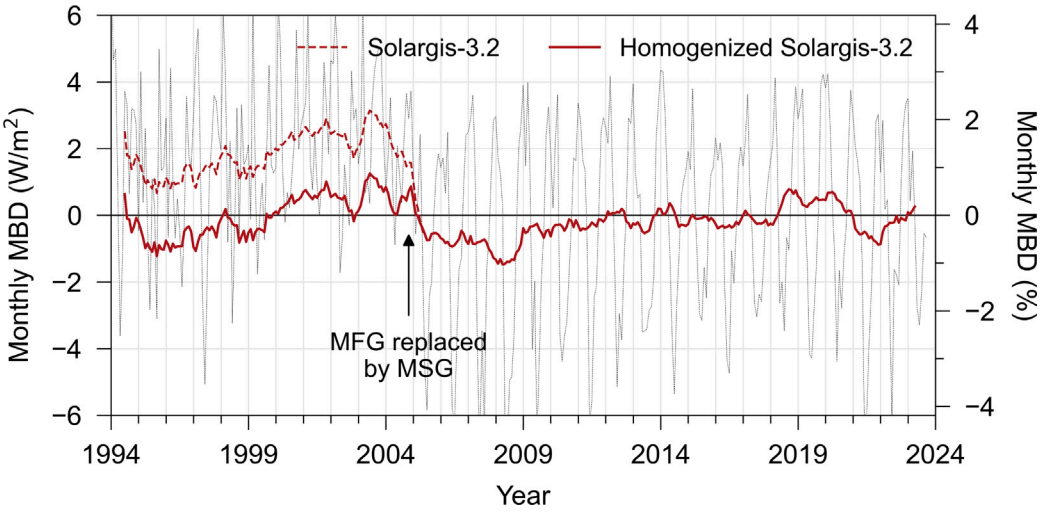

Fig. 2. Monthly MBD of the Solargis-3.2 dataset (grey) in the combined GEBA stations (Table 1) and 12-month running means of the homogenised (solid red) and non-homogenised (dashed red) MBD. The percentage in the right axis is relative to the mean observed SSR in the combined GEBA stations during the Observational period. (For interpretation of the references to colour in this figure legend, the reader is referred to the web version of this article.)

Table 5
Regional SSR trends (in W/m^2/decade) evaluated from the mean anomaly time series of all GEBA locations (GEBA sites) and of all land grid cells (land areas) of the gridded datasets, for the three past periods: Historical, Recent and Observational. The figure after ± is the confidence interval at 95% confidence level. Note that the trend from GEBA observations can only be computed at the GEBA locations. The numbers of land grid cells are: 623,185 for Solargis-3.2, 283,814 for SARAH-3, 11,346 for CLARA-A3, 711 for CEBAF-4.2.1 and 11,488 for ERA5. All trends are significant except in land areas for CLARA-A3 and in the GEBA sites for ERA5.

Dataset	Historical		Recent		Observational[a]	
	GEBA sites	Land areas	GEBA sites	Land areas	GEBA sites	Land areas
GEBA	2.7 ± 1.6		3.0 ± 1.7		3.1 ± 1.0	
Solargis-3.2	2.9 ± 1.8	2.2 ± 1.4	2.9 ± 1.8	3.0 ± 1.5	3.2 ± 1.0	2.6 ± 0.8
SARAH-3	2.5 ± 1.8	2.3 ± 1.4	2.9 ± 1.8	2.3 ± 1.5	3.0 ± 1.0	2.5 ± 0.8
CLARA-A3	1.9 ± 1.8	1.3 ± 1.3	4.3 ± 1.8	4.8 ± 1.5	3.4 ± 1.0	3.1 ± 0.8
CEBAF-4.2.1			2.7 ± 1.6	2.1 ± 1.4	2.9 ± 1.3	2.4 ± 1.0
ERA5	1.1 ± 1.5	1.3 ± 1.1	1.3 ± 1.5	1.4 ± 1.2	1.5 ± 0.9	1.5 ± 0.6

[a] The CEBAF-4.2.1 trends for the Observational period are evaluated only since 2000/03.

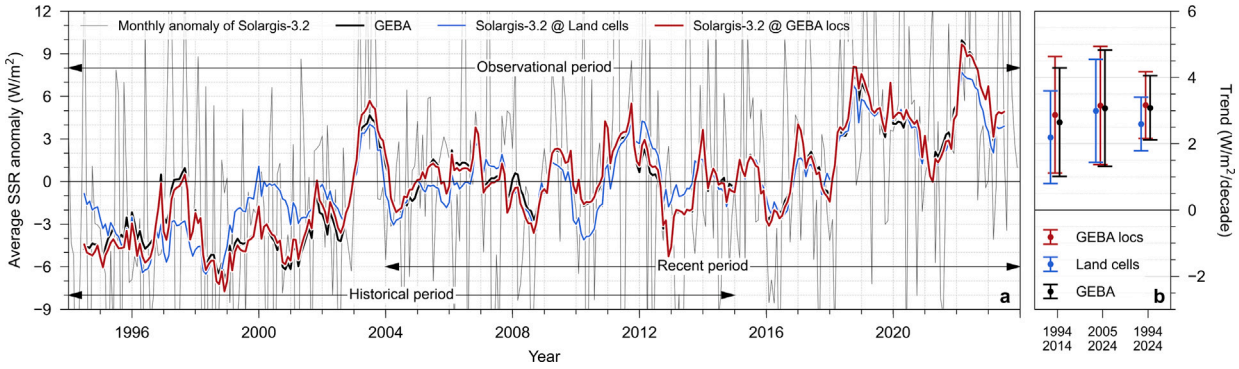

Fig. 3. 12-month running means of (a) regional SSR mean anomalies in the GEBA locations and the land cells of Solargis-3.2 and (b) the SSR trends and confidence interval evaluated from GEBA observations (black) and Solargis-3.2 (red in the GEBA locations, and blue in all land areas) for the Historical, Recent and Observational periods. The vertical bars in panel b are the confidence intervals at the 95% confidence level. (For interpretation of the references to colour in this figure legend, the reader is referred to the web version of this article.)

the Solargis-3.2 and SARAH-3 datasets provide the closest estimates to the observed trends in the GEBA sites, they also likely provide the best estimates for the regional SSR trend in land areas. These estimates are virtually the same for both datasets, 2.6 and 2.5 W/m^2/decade, respectively, during the Observational period.

To illustrate the regional multi-decadal variability of SSR, Fig. 3a shows the mean anomaly time series of the GEBA and Solargis-3.2 datasets; the latter in both the GEBA locations and land areas. As expected, the mean anomaly observed at the GEBA stations is reproduced better when evaluated from the Solargis-3.2 anomaly series at the GEBA locations than when using all grid cells over land areas. In either case, the observed and modelled anomaly time series all follow a common variability pattern: an initial period with an increasing SSR up to about 2005 (when the mean GEBA SSR increases 0.5 W/m^2/year), then a

Table 6
Statistics of the local SSR trends (in W/m^2/decade) evaluated at every GEBA location (GEBA sites) and in the land grid cells of the gridded datasets (land areas), for the three past periods: Historical, Recent and Observational. The figures show the mean SSR trend, and the percentiles 25 and 75 in parenthesis, in each case. Note that the trends from GEBA observations can only be computed at the GEBA locations. The numbers of land grid cells are: 623,185 for Solargis-3.2, 283,814 for SARAH-3, 11,346 for CLARA-A3, 711 for CEBAF-4.2.1 and 11,488 for ERA5.

Dataset	Historical		Recent		Observational[a]	
	GEBA locs	Land cells	GEBA locs	Land cells	GEBA locs	Land cells
GEBA	2.6 (1.5, 3.5)		2.9 (1.2, 4.6)		3.1 (2.5, 3.9)	
Solargis-3.2	2.9 (2.1, 4.2)	2.1 (0.9, 3.6)	3.1 (1.4, 4.7)	3.0 (1.8, 4.3)	3.1 (2.2, 4.2)	2.5 (1.5, 3.8)
SARAH-3	2.5 (1.8, 3.3)	2.3 (1.3, 3.4)	2.8 (1.8, 4.0)	2.3 (1.1, 3.5)	3.0 (2.2, 3.6)	2.5 (1.6, 3.4)
CLARA-A3	1.8 (1.0, 2.4)	1.4 (0.5, 2.3)	4.4 (3.0, 6.2)	4.8 (3.3, 6.2)	3.4 (2.9, 4.0)	3.2 (2.4, 4.0)
CEBAF-4.2.1			2.6 (1.5, 3.9)	2.1 (0.7, 3.5)	2.9 (2.2, 3.7)	2.4 (1.6, 3.3)
ERA5	1.1 (0.5, 1.7)	1.3 (0.0, 2.5)	1.4 (0.3, 2.1)	1.4 (0.3, 2.4)	1.5 (0.7, 2.4)	1.5 (0.7, 2.3)

[a] The CEBAF-4.2.1 trends for the Observational period are evaluated only since 2000/03.

relatively flat period until about 2016 (with a yearly decrease of the mean GEBA SSR of only −0.1 W/m^2/year), and again an increasing SSR trend thereafter (of 0.7 W/m^2/year in the mean GEBA SSR). In Section 4.3, this variability pattern will be related with the 21st century global warming hiatus (Yan et al., 2016). In addition, the SSR anomalies show a few noticeable fluctuations, such as the sudden increase during 2003, probably related to the European heat wave in 2003 (García-Herrera et al., 2010). However, others, such as the large increases in 2018–2020 and 2022, would require further evaluations beyond the scope of this study. Fig. 3b shows the regional SSR trends for the three evaluated periods, with their corresponding confidence intervals, which are much greater than the trend differences.

Alternatively, the regional SSR trend can be aggregated from the local SSR trends evaluated at every GEBA site and, when using the gridded datasets, at every grid cell over land areas as well. The mean regional SSR trends obtained with this approach are shown in Table 6, which, in general, are very similar to those in Table 5. The SSR trend maps for all satellite-based datasets and periods are shown in Fig. 4. All datasets exhibit a generalised increase in SSR between 1994 and 2023 across Europe, with only a few small exceptions in the northern and western Iberian Peninsula during the Recent period and, according to the Solargis-3.2 dataset, also in the north-east of Europe. The spatial distributions of the SSR trends provided by Solargis-3.2 and SARAH-3 are very similar to each other, slightly higher with Solargis-3.2 than with SARAH-3 in the Iberian Peninsula (especially during the Historical and Observational periods) and the northern Mediterranean basin, but smaller in the north-east of Europe. The spatial patterns of CLARA-A3 are similar to those of Solargis-3.2 and SARAH-3 but its trends are generally smaller during the Historical period and higher during the Recent period, as shown also in Table 6. In general, all datasets (including CEBAF-4.2.1 and ERA5) show an overall increase in the mean SSR during the Recent period with respect to the Historical period, which is consistent with the results shown in Fig. 3. However, the maps now additionally show that the increase is primarily produced in central Europe (mainly across north-eastern France, the Benelux and western Germany) and, to a lower extent, in other areas, such as Great Britain, Scandinavia, the Italian Peninsula and the Balkans. The higher SSR increase in central Europe is clearly visible in Fig. 5, which displays higher mean SSR values there during the Recent than during the Historical period by about 3% or more, relative to the mean SSR during the Observational period, in all datasets (more strongly in the Solargis-3.2 and SARAH-3 datasets, and more timidly in CLARA-A3 and ERA5). Although unfortunately there are no GEBA stations fulfilling all the quality criteria right in central Europe, but just in nearby regions (Fig S4), all the gridded datasets agree on the enhancement of SSR in central Europe, which yields certainty about such enhancement.

4.3. Drivers of the SSR trends

This study focusses on the impact of clouds and aerosols, as they have been identified as the two main drivers of long-term trends in SSR, discarding others such as atmospheric water vapour content and solar activity (Wild, 2012; Schilliger et al., 2024).

Table 7
Regional trends of SSR (from GEBA and Solargis-3.2, in W/m^2/decade), SSR by ADE and non-ADE effects (from Solargis-3.2, in W/m^2/decade), AOD (from MERRA-2, in -/decade), CF (from CLARA-A3, in -/decade) and T_{as} (from NOAA, in °C/decade). The trends are evaluated from the mean of all anomalies at the GEBA locations, except for NOAA T_{as}, which is evaluated from the spatially-averaged time series for all Europe (Section 2.4). The value after ± is the confidence interval for 95% confidence level. The mean Solargis-3.2 SSR values during the Historical, Recent and Observational periods are 141, 144 and 143 W/m^2, respectively. The mean CF values are 0.62, 0.60 and 0.61, respectively.

	Historical	Recent	Observational
GEBA	2.7 ± 1.6	3.0 ± 1.7	3.1 ± 1.0
Solargis-3.2	2.9 ± 1.8	3.1 ± 1.8	3.2 ± 1.0
Solargis-3.2 ADE	0.5 ± 1.8	0.9 ± 1.8	0.7 ± 1.0
Solargis-3.2 non-ADE	2.4 ± 1.8	2.2 ± 1.8	2.5 ± 1.0
MERRA-2 AOD	−0.013 ± 0.004	−0.006 ± 0.004	−0.009 ± 0.003
CLARA-A3 CF	−0.023 ± 0.012	−0.012 ± 0.012	−0.020 ± 0.007
NOAA T_{as}	0.41 ± 0.21	0.59 ± 0.22	0.47 ± 0.12

The regional anomalies of SSR (that is, the mean of all anomalies at the GEBA locations) from the simulations of the Solargis-3.2 column model using daily AODs and the monthly AOD climatology are shown in Fig. 6a, and the corresponding decadal trends for the Historical, Recent and Observational periods are provided in Table 7. The trend by ADE, or simply ADE trend, obtained with the Solargis-3.2 dataset (Section 3.4) is always positive, indicating the existence of an underlying decreasing trend in the MERRA-2/MACC-II/CAMS AOD, as it is also shown in Table 7. On average, the ADE trend accounts for 17%, 29% and 22% of the total Solargis-3.2 trend during the Historical, Recent and Observational periods, respectively, being thus noticeably less important than the remaining non-ADE SSR trends combined (83%, 71% and 78%, respectively). Most significantly, the non-ADE trends include impacts related to cloud changes (albedo and coverage) and water vapour absorption. Recently, however, Schilliger et al. (2024) found that, on average, the trend in SSR associated with changes in water vapour absorption during 1983–2020 in Europe was 0.160%/decade. Compared to the contributions that they also found for aerosols and clouds for the same period and region (1.656%/decade and 0.985%/decade, respectively), the contribution of water vapour was considered negligible, in practice. Following these results here, it is assumed that the non-ADE SSR trends are caused by cloud-related changes, thus neglecting the potential impact of water vapour.

The correlation between the monthly regional anomalies of CF and SSR from the Solargis-3.2 column model using the AOD climatology (both shown in Fig. 6) is −89.7%, indicating a strong relationship between the SSR anomaly, excluding the ADE trend, and the CF anomaly. In parallel, the CF anomaly is also significantly correlated (negatively) with the monthly regional T_{as} anomaly (R = −59.1%), which suggests that the reduction in CF might be related to an increase in T_{as}, possibly

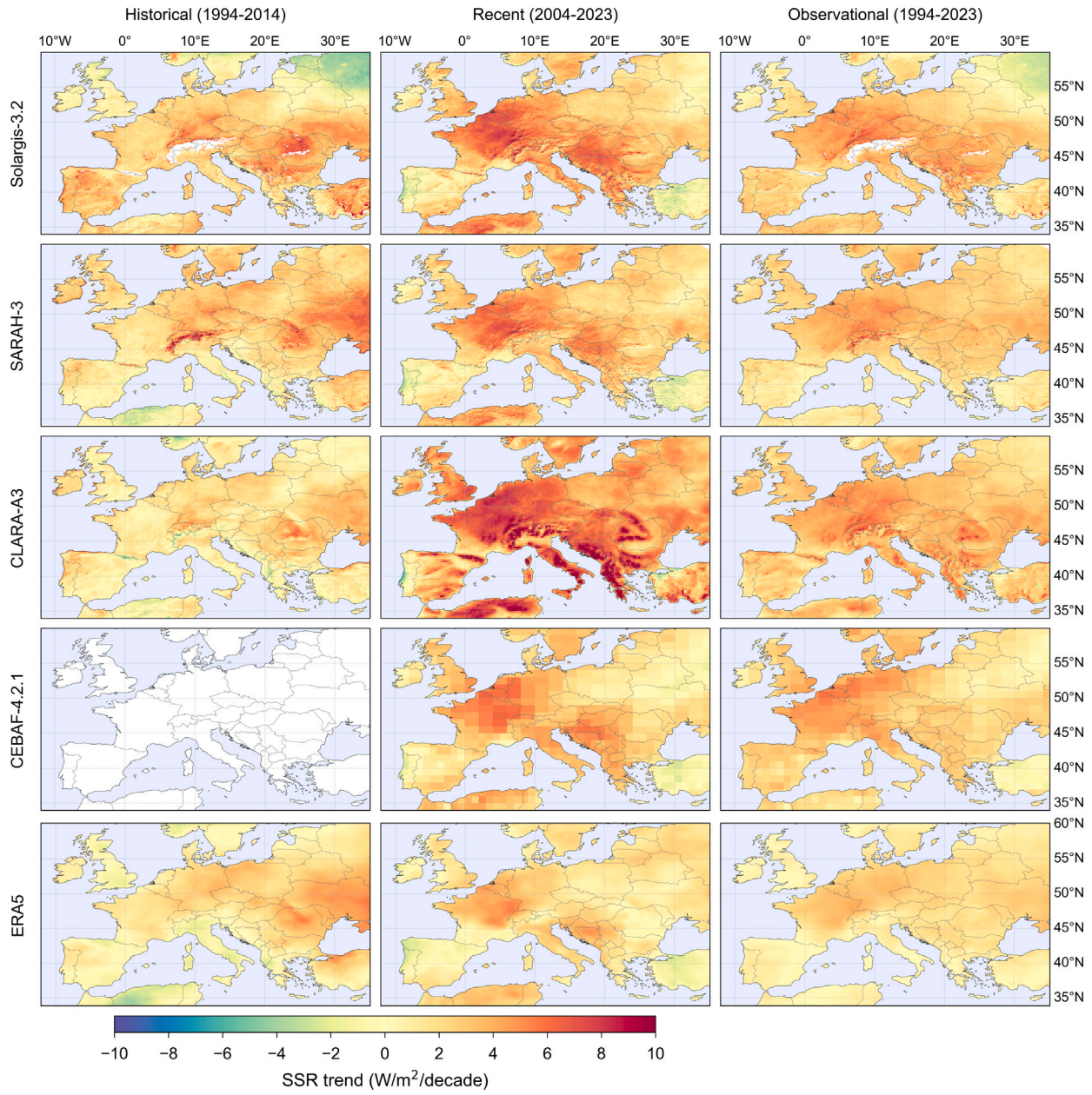

Fig. 4. SSR trend maps for the Historical, Recent and Observational periods (first to third columns, respectively) for the gridded datasets. The maps for Solargis-3.2 during the Historical and Observational periods exclude mountainous areas, where the dataset homogenisation is not valid (see Section 4.1). The map for the CEBAF-4.2.1 dataset during the Historical period is not provided as this dataset starts on March 2000 and the Observational period includes only from that date.

associated with global warming (Schneider et al., 2019). Fig. 6b displays additional evidence of the CF–T_{as} relationship since the increase in T_{as} slows down approximately during the period between 2000 and 2012, during the so-called 21st century global warming hiatus (Yan et al., 2016; Modak and Mauritsen, 2021), coincidentally with a stagnation in the decrease in CF that lasts until approximately the end of the hiatus (Zhang et al., 2019).

If the changes in CF were only produced by changes in T_{as}, the Observational period indicates that, on average, an increase of 0.47 °C in T_{as} reduces CF by 0.02, that is, a rate of ≈ −0.04/°C. This rate of change is higher than others reported in the literature (−0.015/°C in Lu et al., 2023; up to −0.027/°C in McCoy et al., 2017), suggesting that AIE might be also contributing to the increasing SSR trend by reducing cloud albedo (Twomey effect), cloud coverage (Albrecht effect) or both, again under the assumption of negligible impact by water vapour absorption.

A relevant question then is whether the non-ADE SSR trend is only related to changes in CF by T_{as} (hereafter thermal effect, or TE) or is also affected by AIE. To discuss this question, both the first AIE and TE are evaluated using Eqs. (4) and (8), respectively. The evaluation of the first AIE requires the AOD trend. When the MERRA-2 AOD trend for the Recent period (−0.006, from Table 7) is compared against the AOD trend observed at the AERONET stations combined (−0.024), the MERRA-2 trend turns to be four times smaller in magnitude. (The focus is on the Recent period because is the only period with sufficient AERONET stations, as highlighted in Section 2.4). Failing a comprehensive AOD trend validation exercise for MERRA-2, this result suggests that the MERRA-2 AOD cannot represent the regional AOD trend during the Recent period, so the first AIE is here evaluated using only the AERONET trend. It also suggests that the estimated ADE trend (Table 7) might be too small if MACC-II and CAMS also underestimate

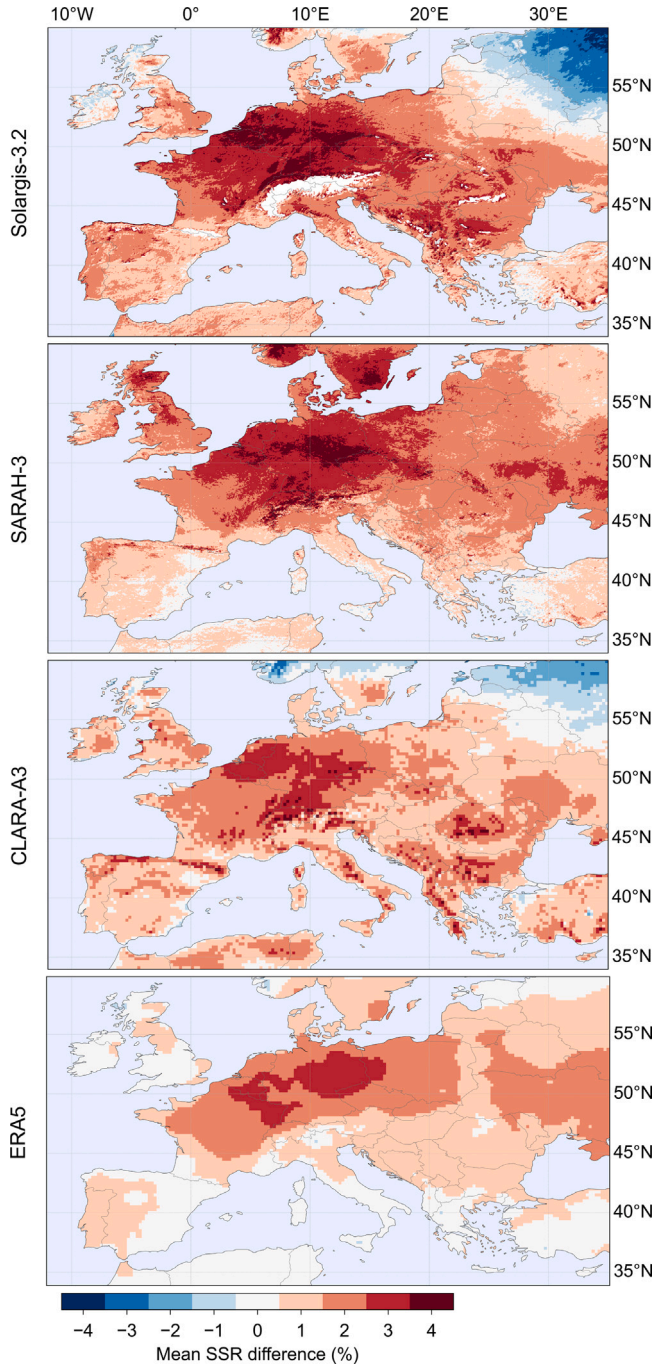

Fig. 5. Difference of the mean SSR during the Recent and Historical periods, in percent with respect to the mean SSR during the Observational period (1994–2023). The map for Solargis-3.2 excludes mountainous areas, where the dataset homogenisation is not valid (see Section 4.1). The CEBAF-4.2.1 dataset is not included because it starts on March 2000.

the AOD trend. However, confirming this would require an additional study which is out of the scope of this work.

The results in Table 8 clearly show that neither the first AIE nor TE alone can explain the non-ADE trend as estimated by the simulations of the Solargis-3.2 column model during the Recent period (2.2 ± 1.8 W/m^2/decade). Only the first AIE could explain the non-ADE trend itself, but only in the very unlikely situations with large α and τ_c, which may be expected for specific cases, but not on average. Therefore, both processes first AIE and TE are most likely contributing

Table 8
Estimates of the first AIE (Eq. (4)) for nine combinations of α and τ_c, and of the SSR trend associated with TE (Eq. (8)). Both are provided in W/m^2/decade. The column f_{AIE} is the fraction of the joint first AIE and TE trends contributed by first AIE. The mean AOD observed at the AERONET stations is 0.16 and a fixed value of 0.80 is selected for the cloud asymmetry parameter for the evaluation of the first AIE. The mean clear-sky index (K_c = 0.66) is evaluated from the outputs of the Solargis-3.2 column model with daily AODs at the GEBA locations. The rest of values needed to evaluate TE are gathered from Table 7.

α	τ_c	First AIE	TE	First AIE+TE	f_{AIE}
0.02	2	0.12	1.09	1.22	0.10
	5	0.22	1.09	1.31	0.16
	8	0.27	1.09	1.36	0.20
0.09	2	0.56	1.09	1.65	0.34
	5	0.97	1.09	2.07	0.47
	8	1.20	1.09	2.29	0.52
0.16	2	0.99	1.09	2.08	0.47
	5	1.73	1.09	2.82	0.61
	8	2.13	1.09	3.22	0.66

to the increase in SSR. It must be noted though that these considerations are made under the assumption that the changes in CF are driven by TE, with all other impacts, such as Albrecht effect, being neglected.

Considering the central case in which α = 0.09 and τ_c = 5, the first AIE + TE trend results in 2.07 W/m^2/decade, which deviates only by 6% from the non-ADE trend value estimated using the Solargis-3.2 column model. The small difference between these two estimates of the non-ADE trend yields robustness and consistency to the two approaches. The fraction of first AIE + TE trend contributed by first AIE varies widely between the two most extreme (α, τ_c) cases. However, with central values, the joint contribution of first AIE and TE to the SSR trend is similar to the non-ADE trend evaluated with the Solargis-3.2 model, while the fractional contribution of the first AIE is about 50%, indicating that, at least during the Recent period, both first AIE and TE might contribute about the same to the non-ADE trend. Therefore, the total SSR trend during the Recent period might be approximately separated into: 30% ADE, 35% first AIE and 35% TE. Assuming that the 50-50 split of first AIE and TE in the non-ADE trend works also for the Observational period, the total SSR trend would approximately separate into: 20% ADE, 40% first AIE and 40% TE.

An additional spatial and temporal qualitative view of the roles of clouds and aerosols in the SSR trend is provided in Fig. 7. The first three rows of panels show the mean CEDS anthropogenic emissions (Fig. 7a–c), the mean MERRA-2 AOD at 550 nm (Fig. 7d–f) and the mean CLARA-A3 CF (Fig. 7g–i) of the Historical, Recent and Observational periods. The anthropogenic emissions are higher in central and, especially, northern Europe (and higher during the Historical than during the Recent period), while AOD is higher in eastern countries (also higher during the Historical than during the Recent period). Note that the MERRA-2 AOD includes natural and anthropogenic sources, as well as atmospheric transport of aerosol particles, which could explain the spatial mismatch with anthropogenic emissions. With regard to CF, it is higher in northern Europe, as expected, especially in central Europe, interestingly where anthropogenic emissions are highest. Again, as for anthropogenic emissions and AOD, it is higher during the Historical period, when emissions are greater than during the Recent period.

Fig. 7j–l shows the mean hygroscopicity parameter, calculated as proposed in Pöhlker et al. (2023) using the aerosol mass fractions of MERRA-2. This parameter accounts for the susceptibility of aerosol particles to act as CCN and is thus related to AIE. All hygroscopicity values in the region are in the approximate range 0.46–0.56, but there are two regions, roughly coincident with France and Romania, with particularly low values, especially during the Recent period.

The remaining panels show the decadal trends for AOD (Fig. 7m–o), CF (Fig. 7p–r) and hygroscopicity parameter (Fig. 7s–u) for each time period. Although MERRA-2 may not be accurate at representing

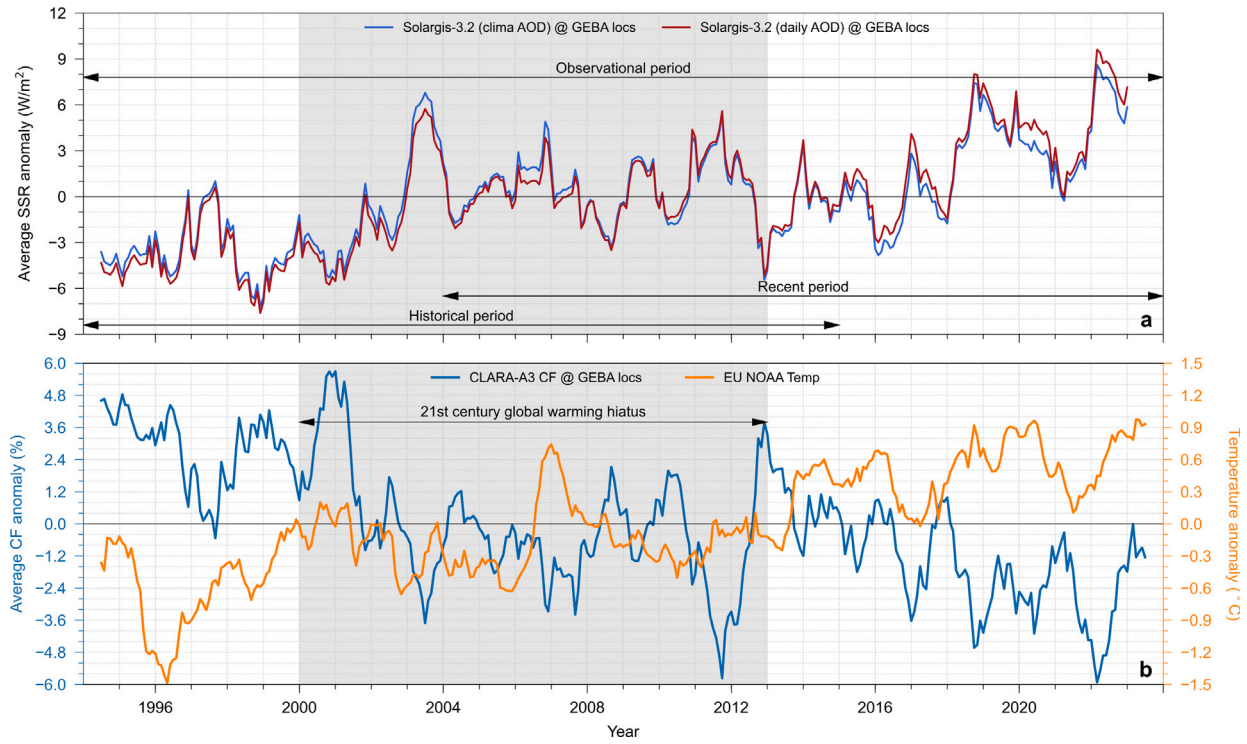

Fig. 6. 12-month running means of the monthly regional SSR anomalies of (a) the Solargis-3.2 column model using daily AODs and the monthly AOD climatology, and (b) CLARA-A3 CF and NOAA T_{as}. All anomalies are evaluated from the mean anomaly in all GEBA locations, except NOAA T_{as}, which is evaluated from the retrieved spatially-averaged anomaly (Section 2.4). The 21st century global warming hiatus period (Yan et al., 2016) is highlighted in grey in the background.

the AOD trends, at least provides an overall view of the sign of the trend and the relative magnitudes between subregions. In general, the study region experienced a relatively uniform decrease in CF, AOD and hygroscopicity during the Observational period, with the only major exception of the Iberian Peninsula and Anatolia for AOD. However, it is important to note that the decreasing trends in AOD were stronger in the northern Balkans, and the decreasing trends in hygroscopicity were stronger in France and some other spotted regions.

When the spatial and temporal patterns of all these variables are compared to Figs. 4 and 5, they show that the SSR trends cannot be generally explained only by changes in aerosols or changes in clouds, as has been concluded also from the analysis of AIE and TE. For instance, the positive trends of SSR in the Iberian Peninsula and Anatolia during the Observational period are most likely due to a decrease in CF, since AOD remained reasonably stable during this period. The hygroscopicity also decreased slightly, which might have also contributed to the decrease in cloudiness. In contrast, the high positive trends in SSR in northern France, Benelux, Germany and northern Balkans are most likely due to a combined impact of aerosols and clouds. However, the contribution of aerosols is probably not limited only to the mere extinction of SSR because the reduction of the hygroscopicity parameter points towards a decrease in the aerosol contribution to the formation of clouds, which could partially explain the reduction of CF in France during the Observational period. However, the hygroscopicity parameter only accounts for the susceptibility of aerosol particles to act as CCN. In addition, the amount of aerosol particles (proportional to AOD) must also be considered because a reduction of such an amount is more critical in low polluted areas than in highly polluted areas (Wild, 2009), as might be comparatively the case of France and northern Balkans (Fig. 7f), where the relative impact of SSR extinction by aerosols is probably more important than in France. The Iberian Peninsula is another interesting example because it has modest AOD values around 0.10–0.12, and CF is expected to be sensitive to changes in AOD, to some extend. In particular, during the Historical period, there is a generalised decrease in AOD and CF. Thereafter, in the Recent period, AOD stabilises, or even rises in central and western Iberia, while keeps decreasing slightly in the Mediterranean southern coast. Interestingly, CF during the Recent period follows a quite similar variability pattern: decreasing in the south and increasing in western, central and also northern areas. In addition to the aerosol direct and indirect effects, the increase of surface temperatures might also play a significant role, as discussed earlier.

4.4. Projected SSR trends

Fig. 8 shows the regional SSR trends obtained from the average anomaly of the CMIP6 predictions at the GEBA locations for all, clear and cloudy sky conditions (referred to as all-sky, clear and cloudy trends, respectively) for the Historical (1994–2014) and Projected (2024–2054) periods.

The spread of the CMIP6 ensemble (CE) trends for the Historical period is much greater than for the SSP scenarios under any sky conditions, which is consequence of the stiff forcings imposed by the simulation scenarios (O'Neill et al., 2016). The spread of the clear trends is always smaller than for cloudy trends, suggesting a greater modelling uncertainty in the simulation of cloudy conditions.

The median regional trend of the CE during the Historical period under all sky conditions is 1.8 W/m^2/decade, while the regional SSR trend evaluated from the GEBA observations is 2.7 W/m^2/decade. It corresponds to the percentile 75 of the CE, indicating a noticeable tendency of its members to underestimate the observed trend. The Historical median clear and cloudy trends of the ensemble are 1.2 and 0.5 W/m^2/decade, respectively. Hence, a 67% of the all-sky median trend is due to clear sky conditions. Assuming a negligible impact of water vapour absorption in the SSR trend, the ADE trend determined in Section 4.3 should be similar to the clear trend. Therefore, the relative magnitude found for the CE clear trend (67%) is in stark disagreement with the findings in Section 4.3, which estimated 17% for the Historical period, and suggests that the CE overestimates (underestimates) the relative importance of the clear (cloudy) SSR trend. Nonetheless, as also

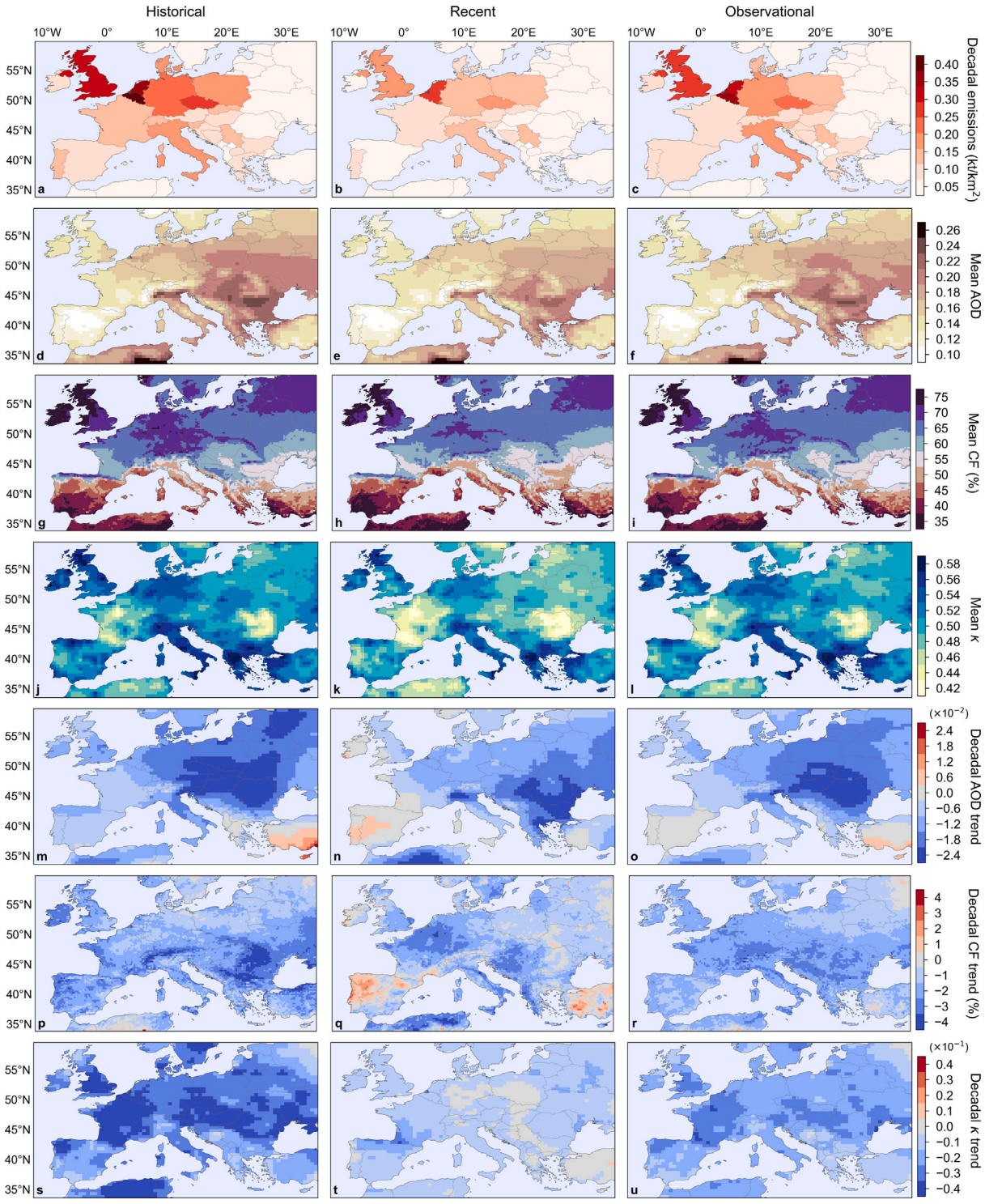

Fig. 7. Mean CEDS anthropogenic emissions (a–c), MERRA-2 AOD (d–f), CLARA-A3 CF (g–i) and hygroscopicity parameter (j–l), and decadal trends of MERRA-2 AOD (m–o), CLARA-A3 CF (p–r) and hygroscopicity parameter (s–u) during the Historical, Recent and Observational periods in the study region. The CEDS emissions include black and organic carbon and secondary organic and inorganic aerosol compounds.

shown in Section 4.3, the estimate of the ADE trend might be too low as the modelled AOD trend by MERRA-2/MACC-II/CAMS might also be too low.

The projected SSR trends show small differences between forcings scenarios for all sky conditions, with the maximum median trend occurring for SSP1-2.6 (0.8 W/m^2/decade) and the minimum for SSP5-8.5 (0.2 W/m^2/decade), and without evident systematic dependency on the forcings severity. In contrast, the median trend of the ensemble decreases with the severity of the forcings for clear conditions, becoming −0.5 W/m^2/decade for SSP5-8.5. The opposite occurs for cloudy conditions, when the median trend is positive and increases with the severity of the forcing scenario. While the findings for the median clear trends are somewhat expected, since an increase in anthropogenic emissions is expected to lead to higher aerosol extinction rates, the

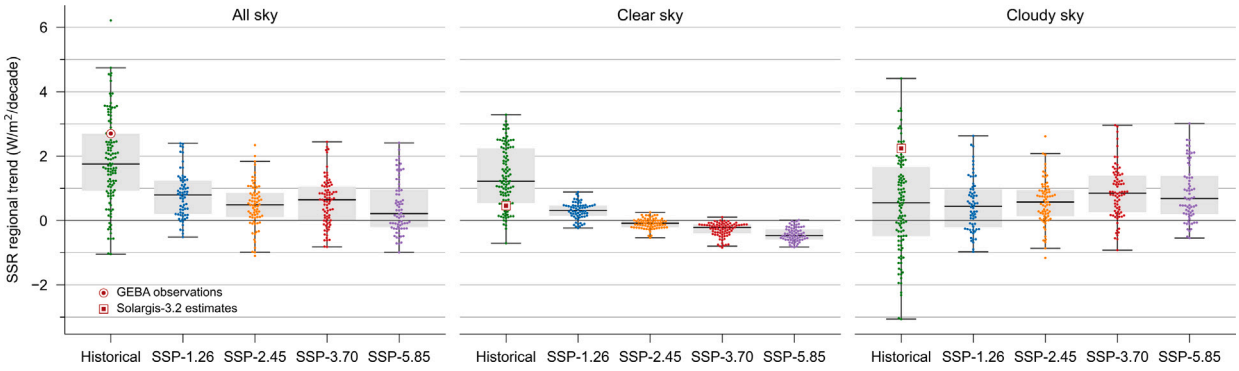

Fig. 8. Regional SSR trends (dots) for all sky, clear sky and cloud sky conditions from the CMIP6 ensemble models. The all and clear sky trends are evaluated from the mean anomalies of SSR and clear-sky SSR, respectively, at all the GEBA locations. The cloudy sky trends are evaluated from the difference between all sky and clear sky trends. The trends are shown for the Historical period (coincidently with the CMIP6 Historical simulations) and for the Projected period (coincidently with for the CMIP6 simulations of SSP scenarios). The grey boxes in the background are boxplots of the SSR trends. The upper and lower bounds of the boxes extend from the lower to the upper quartiles and the whiskers extend 1.5 times the inter-quartile range from the box. The ensemble median is shown as a black horizontal line within the boxes. The Solargis-3.2 trends are the ADE trend in the clear sky panel and the non-ADE trend in the cloudy sky panel.

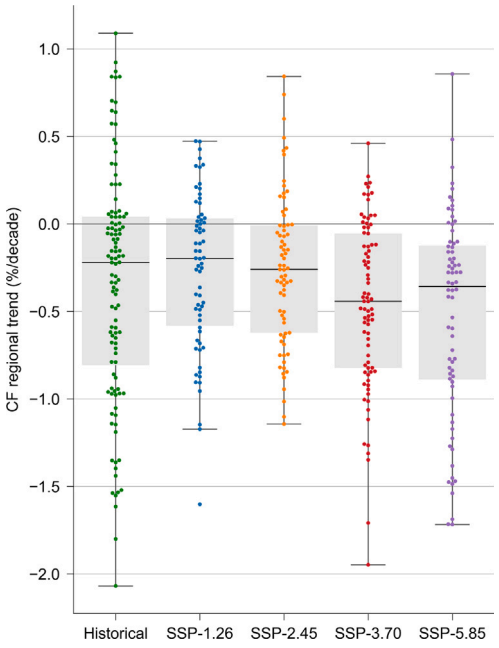

Fig. 9. As Fig. 8, but for the CMIP6 CF.

increasing median trend in SSR for cloudy conditions indicates a reduction of CF and/or an increase in the transparency of clouds, apparently contradicting the expected effects of greater availability of CCN in the atmosphere. In particular, Fig. 9 shows that CF actually decreases in more severe forcing scenarios, except for SSP5-8.5, whose CF trend is smaller (in magnitude) than for SSP3-7.0, which might indicate stagnation or saturation in the CF reduction. This situation points, again, to a probable impact of TE under rising temperatures (Carvalho et al., 2021).

Fig. 10 shows the spatial distribution of the median all-sky SSR trends in the study region. The trend is positive everywhere, for the Historical period and in all SSP scenarios. In general, the trends during the Historical period are smaller than those evaluated from the gridded historical datasets (left column of Fig. 4), and the trends for the SSP scenarios are even smaller. In all cases, the spatial distribution of the trends is very uniform, at least, compared to the results shown in Fig. 4.

5. Discussion and conclusions

SSR observations at ground radiometric sites are prone to errors, and thus require quality assurance protocols that, unfortunately, cannot always be applied. This limitation is particularly important for the evaluation of multidecadal trends because trends are very sensitive to data inhomogeneities and, without proper quality assurance, inhomogeneities are likely to occur. Although such inhomogeneities in observed data can, in principle, be detected, they are difficult to correct. As an example, for the GEBA stations considered here, standard homogeneity tests detected at least one point of change in most of the sitewise datasets. Hence, SSR trends are expected to carry uncertainties related to inherent inhomogeneities when they are computed from ground observations at single locations. Observations at ground stations are, however, best suited combined with other ground stations' data to evaluate a wide-area, or regional, estimate of the SSR trend because the potential inhomogeneities are often independent among stations, especially if the ground stations belong to different observational networks and follow independent maintenance programs.

Satellite-based SSR datasets provide spatially distributed SSR data with a quality that, at the monthly scale, is generally comparable to that of ground observations (≈5% standard uncertainty). They are thus a valuable data source to provide spatially continuous SSR trends. However, as ground data, satellite-based datasets are potentially affected by data inhomogeneities, which, for them, is a particularly critical issue because they typically provide their estimates based on a single, or only a few, spaceborne spectroradiometers. Hence, any issue with the sensors unavoidably spreads across the entire sensed area, and ensuring the homogeneity of these data is crucial to guarantee the validity of their results. Thus, there must be a synergetic co-existence of ground- and satellite-based data: the ground data ensure the temporal stability of the satellite data, and the satellite data expand the spatial context of the ground data.

Here, five gridded SSR datasets have been considered, four of them primarily based, to a greater or lesser extent, on observations from spaceborne spectroradiometers (Solargis-3.2, SARAH-3, CLARA-A3 and CEBAF-4.2.1), and an atmospheric reanalysis dataset (ERA5). Among them, Solargis-3.2 has the smallest root mean square deviation (6.39 W/m^2) with respect to the SSR observations at the GEBA locations throughout the evaluation period 1994–2023. However, it also presents a stability breakpoint due to the replacement of the Meteosat First Generation by the Meteosat Second Generation. Once corrected, Solargis-3.2 and SARAH-3 were the models with the closest estimates to the observed regional SSR trends for the Historical, Recent and Observational periods (2.7, 3.0 and 3.1 W/m^2/decade, respectively),

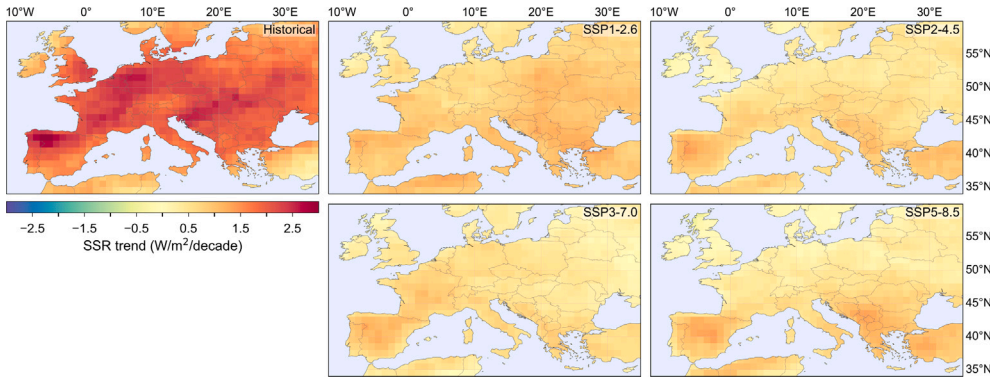

Fig. 10. Median SSR trend of the CMIP6 ensemble for the Historical period and the four SSP scenarios. All maps share the colour scale. Before computing the trends, all CMIP6 ensemble members were regridded to a common 1° × 1° grid using a conservative scheme. If these maps are compared to those in Fig. 4, be aware of the different colour scale. (For interpretation of the references to colour in this figure legend, the reader is referred to the web version of this article.)

always within a difference of ±0.2 W/m^2/decade with respect to GEBA. The ERA5 reanalysis always underestimates by more than 50% the observed SSR trend.

All datasets exhibit a generalised increase in SSR between 1994 and 2023 throughout Europe. Compared to the Historical period, all datasets show an overall increase in the mean SSR during the Recent period. The SSR trend maps indicate that the increase is primarily produced in Central Europe (mainly in northeastern France, the Benelux and western Germany) and, to a lower extent, in other areas, such as Great Britain, Scandinavia, the Italian Peninsula and the Balkans.

Long-term trends in SSR are primarily originating from changes in clouds and aerosols. Neglecting other potential sources of SSR trends (such as changes in solar activity or in water vapour), and using a column version of the Solargis-3.2 model that has been run at the GEBA locations using alternatively inputs of daily AOD and a long-term monthly climatology of AOD from MERRA-2, MACC-II and CAMS, the fraction of the trend attributable to ADE is quantified in 17%, 29% and 22% for the Historical, Recent and Observational periods, respectively. This result indicates that ≈20% of the trend of SSR in Europe in the period 1994–2023 is due to ADE and that the remaining ≈80% relate to changes in clouds. The secondary role of aerosol extinction is aligned with the excellent predictions of the SSR trends made by satellite-based gridded SSR datasets that use prescribed aerosol climatologies, such as SARAH-3 and CLARA-A3. However, the impact of aerosols is not limited to ADE, as deduced from a sensitivity analysis that quantifies the impact of the first AIE in SSR close to 1% (of the mean SSR). It turns out, however, that the first AIE is not enough to explain the cloudy SSR trend, and it has been shown that the increase of surface temperatures within the context of global warming might be contributing to the cloudy trend as well. Overall, taking the Recent period as a reference, because it has a better characterisation of the regional AOD in the AERONET network, the SSR trend during the Observational period would be roughly produced in 1/5 by ADE, 2/5 by first AIE and 2/5 by change in air temperature. That is, the cloud-related changes would be twice as much important as ADE at the regional scale.

The regional SSR trend observed during the Historical period (2.7 W/m^2/decade) is the percentile 75 of the SSR trends predicted by the CMIP6 ensemble, which indicates a noticeable underestimating tendency in its members. The median SSR trend under clear (cloudy) conditions is 67% (33%) of that under all sky conditions, which is in stark contrast with the previous findings, which quantify the clear trend in ≈17% of the all sky trend. This suggests that the CMIP6 ensemble strongly overestimates (underestimates) the relative importance of the clear (cloudy) trend.

The median SSR trends projected by the CMIP6 ensemble for the period 2024–2054 for clear sky conditions decrease (and become negative) with the severity of the forcings (i.e., from SSP1-2.6 to SSP5-8.5) and increase for cloudy conditions. These opposing tendencies counterbalance for all sky conditions and preclude any significant dependency with the forcing scenario, always taking positive values and smaller than 1 W/m^2/decade. In parallel, CF decreases with increasing forcing severity, explaining the increase in SSR under cloudy conditions, and suggests a potential impact of increasing temperatures in the suppression of clouds.

Last but not less important, this study presents limitations that should be considered for a correct interpretation of its results. First, the estimation of ADE is based on the AOD trend modelled by MERRA-2, MACC-II and CAMS throughout 1994–2024. The comparison of the MERRA-2 AOD trend during the Recent period to that obtained from AERONET observations carried out in Section 4.3 suggests that the modelled AOD trends might significantly underestimate the magnitude of the observed decreasing multi-decadal AOD trend. The relative importance of ADE would then be greater than that determined here. Second, the evaluations performed here neglect the contribution of water vapour absorption in the SSR trend, based on the results of Schilliger et al. (2024). However, this assumption should be carefully evaluated in future studies, as recent works have reported significant trends in water vapour in Europe (1.7–5.0%/decade during 1994–2018; Yuan et al., 2023a). Third, with respect to AIE, the Twomey effect has been considered assuming central values of cloud optical depth, while the Albrecht effect has been neglected. This assumption ignores the potential impact of aerosols on cloud coverage, despite recent strong evidence (Yuan et al., 2023b), and has left the modelling of the impact of cloud coverage only to the changes in air temperature.

Future works should consider the use of a gridded dataset that provides unbiased AOD trends, probably integrating ground AERONET observations and modelled datasets, to improve the estimate of ADE and non-ADE trends. The improved AOD dataset would help to find a better effective cloud optical depth to also improve the evaluation of the first AIE. The role of water vapour should be considered to find a better estimate of the clear trend, as it should be considered the second AIE too, as a previous step to address the mutual feedback between cloud coverage and air temperature (Loeb et al., 2025; Goessling et al., 2025; Schneider et al., 2019).

CRediT authorship contribution statement

Leandro C. Segado-Moreno: Writing – review & editing, Methodology, Formal analysis, Data curation, Conceptualization. **José A. Ruiz-Arias:** Writing – review & editing, Writing – original draft, Methodology, Formal analysis, Data curation, Funding acquisition, Conceptualization. **Juan Pedro Montávez:** Writing – review & editing, Funding acquisition, Conceptualization. **Juraj Betak:** Writing – review & editing, Formal analysis, Data curation.

Declaration of competing interest

The authors declare that they have no known competing financial interests or personal relationships that could have appeared to influence the work reported in this paper.

Acknowledgements

GEBA is co-funded by the Federal Office of Meteorology and Climatology MeteoSwiss within the framework of GCOS Switzerland. We acknowledge the World Radiation Data Center for sharing ground data and the World Climate Research Program, which, through its Working Group on Coupled Modelling, coordinated and promoted CMIP6. We thank the climate modelling groups for producing and making available their model output, the Earth System Grid Federation (ESGF) for archiving the data and providing access, and the funding agencies who support CMIP6 and ESGF. The authors are grateful to Solargis s.r.o., the Climate Application Facility on Climate Monitoring of EUMETSAT, the ECMWF and the Copernicus Climate Data Store, the Atmospheric Science Data Center and the Global Modelling and Assimilation Office at NASA for providing the SSR, CF and aerosol datasets, the National Oceanic and Atmospheric Administration for providing temperature data, and the Aerosol Robotics Network and CEDS personnel and scientists for kindly sharing the AOD and anthropogenic emissions datasets. J.A. Ruiz-Arias was supported by the projects PID2019-107455RB-C21 and PID2023-149827OB-C21 funded by MCIU/AEI/10.13039/501100011033 and FSE+, and the project UMA20-FEDERJA-134 jointly funded by the FEDER 2014–2020 Operative Program and the Consejería de Economía, Conocimiento, Empresas y Universidad of the Junta de Andalucía. L.C. Segado-Moreno and J.P. Montávez were supported by the project ECCE (PID2020-115693RB-I00) financed by the Spain Ministry of Science and Innovation. L.C. Segado-Moreno thanks the predoctoral contract FPI (PRE2021-099236) from Spanish Ministry of Science and Innovation. The University of Málaga/CBUA provided the funding for open access.

Appendix A. Supplementary data

Supplementary material related to this article can be found online at https://doi.org/10.1016/j.rse.2025.115122.

Data availability

Data will be made available on request.

References

Albrecht, B.A., 1989. Aerosols, cloud microphysics, and fractional cloudiness. Sci. 245 (4923), 1227–1230. http://dx.doi.org/10.1126/science.245.4923.1227.

Alexandersson, H., 1986. A homogeneity test applied to precipitation data. J. Climatol. 6 (6), 661–675. http://dx.doi.org/10.1002/joc.3370060607.

Allen, R.J., Amiri-Farahani, A., Lamarque, J.-F., Smith, C., Shindell, D., Hassan, T., Chung, C.E., 2019. Observationally constrained aerosol–cloud semi-direct effects. Npj Clim. Atmospheric Sci. 2 (1), http://dx.doi.org/10.1038/s41612-019-0073-9.

Augustine, J.A., Dutton, E.G., 2013. Variability of the surface radiation budget over the United States from 1996 through 2011 from high-quality measurements. J. Geophys. Res.: Atmospheres 118 (1), 43–53. http://dx.doi.org/10.1029/2012JD018551.

Bartók, B., Wild, M., Folini, D., Lüthi, D., Kotlarski, S., Schär, C., Vautard, R., Jerez, S., Imecs, Z., 2017. Projected changes in surface solar radiation in CMIP5 global climate models and in EURO-CORDEX regional climate models for Europe. Clim. Dyn. 49 (7), 2665–2683. http://dx.doi.org/10.1007/s00382-016-3471-2.

Bellouin, N., Yu, H., 2022. Aerosol–radiation interactions. In: Aerosols and Climate. Elsevier, pp. 445–487. http://dx.doi.org/10.1016/b978-0-12-819766-0.00004-3, chapter 11.

Buishand, T., 1982. Some methods for testing the homogeneity of rainfall records. J. Hydrol. 58 (1–2), 11–27. http://dx.doi.org/10.1016/0022-1694(82)90066-x.

Cano, D., Monget, J.-M., Albuisson, M., Guillard, H., Regas, N., Wald, L., 1986. A method for the determination of the global solar radiation from meteorological satellite data. Sol. Energy 37 (1), 31–39. http://dx.doi.org/10.1016/0038-092X(86)90104-0.

Carvalho, D., Cardoso Pereira, S., Rocha, A., 2021. Future surface temperatures over Europe according to CMIP6 climate projections: an analysis with original and bias-corrected data. Clim. Change 167 (1–2), http://dx.doi.org/10.1007/s10584-021-03159-0.

Chtirkova, B., Folini, D., Correa, L.F., Wild, M., 2022. Internal variability of all-sky and clear-sky surface solar radiation on decadal timescales. J. Geophys. Res.: Atmospheres 127 (12), http://dx.doi.org/10.1029/2021jd036332.

CMIP, 2025. World climate research programme's coupled model intercomparison project. https://wcrp-cmip.org. (Accessed 29 April 2025).

Dürr, B., Zelenka, A., 2009. Deriving surface global irradiance over the Alpine region from METEOSAT Second Generation data by supplementing the HELIOSAT method. Int. J. Remote Sens. 30 (22), 5821–5841. http://dx.doi.org/10.1080/01431160902744829.

Eyring, V., Bony, S., Meehl, G.A., Senior, C.A., Stevens, B., Stouffer, R.J., Taylor, K.E., 2016. Overview of the coupled model intercomparison project phase 6 (CMIP6) experimental design and organization. Geosci. Model. Dev. 9 (5), 1937–1958. http://dx.doi.org/10.5194/gmd-9-1937-2016.

Fang, H., Qin, W., Wang, L., Zhang, M., Yang, X., 2020. Solar brightening/dimming over China's mainland: Effects of atmospheric aerosols, anthropogenic emissions, and meteorological conditions. Remote. Sens. 13 (1), 88. http://dx.doi.org/10.3390/rs13010088.

Feingold, G., Eberhard, W.L., Veron, D.E., Previdi, M., 2003. First measurements of the Twomey indirect effect using ground-based remote sensors. Geophys. Res. Lett. 30 (6), http://dx.doi.org/10.1029/2002gl016633.

Forstinger, A., Wilbert, S., Jensen, A.R., Kraas, B., Peruchena Fernández, C., Gueymard, C.A., Ronzio, D., Yang, D., Collino, E., Polo Martinez, J., Ruiz-Arias, J.A., Hanrieder, N., Blanc, P., Saint-Drenan, Y.-M., 2023. Worldwide Benchmark of Modelled Solar Irradiance Data. Tech. Report T16-05:2023, International Energy Agency, Photovoltaic Power Systems Programme (IEA PVPS).

Gao, Z., Ye, D., Ma, Q., 2025. Aerosols drive the missed global brightening recently in ERA5 and ERAI over Japan. Q. J. R. Meteorol. Soc. http://dx.doi.org/10.1002/qj.70011.

García-Herrera, R., Díaz, J., Trigo, R.M., Luterbacher, J., Fischer, E.M., 2010. A review of the European summer heat wave of 2003. Crit. Rev. Environ. Sci. Technol. 40 (4), 267–306. http://dx.doi.org/10.1080/10643380802238137.

Gelaro, R., McCarty, W., Suárez, M.J., Todling, R., Molod, A., Takacs, L., Randles, C.A., Darmenov, A., Bosilovich, M.G., Reichle, R., et al., 2017. The modern-era retrospective analysis for research and applications, version 2 (MERRA-2). J. Clim. 30 (14), 5419–5454. http://dx.doi.org/10.1175/JCLI-D-16-0758.1.

Giles, D.M., Sinyuk, A., Sorokin, M.G., Schafer, J.S., Smirnov, A., Slutsker, I., Eck, T.F., Holben, B.N., Lewis, J.R., Campbell, J.R., Welton, E.J., Korkin, S.V., Lyapustin, A.I., 2019. Advancements in the Aerosol Robotic Network (AERONET) version 3 database – automated near-real-time quality control algorithm with improved cloud screening for Sun photometer aerosol optical depth (AOD) measurements. Atmospheric Meas. Tech. 12 (1), 169–209. http://dx.doi.org/10.5194/amt-12-169-2019.

Gilgen, H., Ohmura, A., 1999. The global energy balance archive. Bull. Am. Meteorol. Soc. 80 (5), 831–850. http://dx.doi.org/10.1175/1520-0477(1999)080<0831:TGEBA>2.0.CO;2.

GMAO, 2015. MERRA-2 tavgM_2d_aer_Nx: 2d, Monthly mean, Time-averaged, Single-Level, Assimilation, Aerosol Diagnostics V5.12.4. Global Modeling And Assimilation Office, NASA Goddard Earth Sciences Data and Information Services Center, http://dx.doi.org/10.5067/FH9A0MLJPC7N, URL: https://disc.gsfc.nasa.gov/datacollection/M2TMNXAER_5.12.4.html.

Goessling, H.F., Rackow, T., Jung, T., 2025. Recent global temperature surge intensified by record-low planetary albedo. Sci. 387 (6729), 68–73. http://dx.doi.org/10.1126/science.adq7280.

Gueymard, C.A., 2014. A review of validation methodologies and statistical performance indicators for modeled solar radiation data: Towards a better bankability of solar projects. Renew. Sustain. Energy Rev. 39, 1024–1034. http://dx.doi.org/10.1016/j.rser.2014.07.117.

He, Y., Yang, K., Wild, M., Wang, K., Tong, D., Shao, C., Zhou, T., 2022. Constrained future brightening of solar radiation and its implication for China's solar power. Natl. Sci. Rev. 10 (1), http://dx.doi.org/10.1093/nsr/nwac242.

Hersbach, H., Bell, B., Berrisford, P., Hirahara, S., Horányi, A., Muñoz-Sabater, J., Nicolas, J., Peubey, C., Radu, R., Schepers, D., et al., 2020. The ERA5 global reanalysis. Q. J. R. Meteorol. Soc. 146 (730), 1999–2049. http://dx.doi.org/10.1002/qj.3803.

Hoesly, R., Smith, S.J., Ahsan, H., Prime, N., O'Rourke, P., Crippa, M., Klimont, Z., Guizzardi, D., Feng, L., Harkins, C., MCDONALD, B., Wang, S., 2025. CEDS v_2025_03_18 aggregate data. http://dx.doi.org/10.5281/zenodo.15059443.

Hoesly, R.M., Smith, S.J., Feng, L., Klimont, Z., Janssens-Maenhout, G., Pitkanen, T., Seibert, J.J., Vu, L., Andres, R.J., Bolt, R.M., Bond, T.C., Dawidowski, L., Kholod, N., Kurokawa, J.-i., Li, M., Liu, L., Lu, Z., Moura, M.C.P., O'Rourke, P.R., Zhang, Q., 2018. Historical (1750–2014) anthropogenic emissions of reactive gases and aerosols from the Community Emissions Data System (CEDS). Geosci. Model. Dev. 11 (1), 369–408. http://dx.doi.org/10.5194/gmd-11-369-2018.

Hussain, M.M., Mahmud, I., Bari, S.H., 2023. pyHomogeneity: A python package for homogeneity test of time series data. J. Sea Res. 11, http://dx.doi.org/10.5334/jors.427.

Ineichen, P., 2008. A broadband simplified version of the Solis clear sky model. Sol. Energy 82 (8), 758–762. http://dx.doi.org/10.1016/j.solener.2008.02.009.

Ineichen, P., 2013. Long Term Satellite Hourly, Daily and Monthly Global, Beam and Diffuse Irradiance Validation. Interannual Variability Analysis. Technical Report, Université de Geneve, URL: https://archive-ouverte.unige.ch/unige:29606.

Ineichen, P., 2018. High turbidity solis clear sky model: development and validation. Remote Sens. 10 (3), 435. http://dx.doi.org/10.3390/rs10030435.

Inness, A., Ades, M., Agustí-Panareda, A., Barré, J., Benedictow, A., Blechschmidt, A.-M., Dominguez, J.J., Engelen, R., Eskes, H., Flemming, J., et al., 2019. The CAMS reanalysis of atmospheric composition. Atmospheric Chem. Phys. 19 (6), 3515–3556. http://dx.doi.org/10.5194/acp-19-3515-2019.

Inness, A., Baier, F., Benedetti, A., Bouarar, I., Chabrillat, S., Clark, H., Clerbaux, C., Coheur, P., Engelen, R., Errera, Q., et al., 2013. The MACC reanalysis: an 8 yr data set of atmospheric composition. Atmospheric Chem. Phys. 13 (8), 4073–4109. http://dx.doi.org/10.5194/acp-13-4073-2013.

Jerez, S., Tobin, I., Vautard, R., Montávez, J.P., López-Romero, J.M., Thais, F., Bartok, B., Christensen, O.B., Colette, A., Déqué, M., et al., 2015. The impact of climate change on photovoltaic power generation in Europe. Nat. Commun. 6 (1), 10014. http://dx.doi.org/10.1038/ncomms10014.

Kalogirou, S.A., 2013. Solar Energy Engineering: Processes and Systems. Academic Press, pp. 49–762.

Karlsson, K.-G., Riihelä, A., Trentmann, J., Stengel, M., Solodovnik, I., Meirink, J.F., Devasthale, A., Jääskeläinen, E., Kallio-Myers, V., Eliasson, S., Benas, N., Johansson, E., Stein, D., Finkensieper, S., Håkansson, N., Akkermans, T., Clerbaux, N., Selbach, N., Marc, S., Hollmann, R., 2023a. CLARA-A3: CM SAF cLoud, Albedo and surface RAdiation dataset from AVHRR data - Edition 3. http://dx.doi.org/10.5676/EUM_SAF_CM/CLARA_AVHRR/V003, URL: https://wui.cmsaf.eu/safira/action/viewDoiDetails?acronym=CLARA_AVHRR_V003.

Karlsson, K.-G., Stengel, M., Meirink, J.F., Riihelä, A., Trentmann, J., Akkermans, T., Stein, D., Devasthale, A., Eliasson, S., Johansson, E., Håkansson, N., Solodovnik, I., Benas, N., Clerbaux, N., Selbach, N., Schröder, M., Hollmann, R., 2023b. CLARA-A3: The third edition of the AVHRR-based CM SAF climate data record on clouds, radiation and surface albedo covering the period 1979 to 2023. Earth Syst. Sci. Data 15 (11), 4901–4926. http://dx.doi.org/10.5194/essd-15-4901-2023.

Kato, S., Rose, F.G., Rutan, D.A., Thorsen, T.J., Loeb, N.G., Doelling, D.R., Huang, X., Smith, W.L., Su, W., Ham, S.-H., 2018. Surface irradiances of edition 4.0 clouds and the earth's radiant energy system (CERES) energy balanced and filled (EBAF) data product. J. Clim. 31 (11), 4501–4527. http://dx.doi.org/10.1175/jcli-d-17-0523.1.

Kendall, M.G., Gibbons, J.D., 1990. Rank Correlation Methods. Oxford University Press.

Kokhanovsky, A., 2004. Optical properties of terrestrial clouds. Earth-Sci. Rev. 64 (3–4), 189–241. http://dx.doi.org/10.1016/s0012-8252(03)00042-4.

Liang, S., Fang, H., Chen, M., Shuey, C.J., Walthall, C., Daughtry, C., Morisette, J., Schaaf, C., Strahler, A., 2002. Validating MODIS land surface reflectance and albedo products: methods and preliminary results. Remote Sens. Environ. 83 (1–2), 149–162. http://dx.doi.org/10.1016/s0034-4257(02)00092-5.

Loeb, N.G., Doelling, D.R., Wang, H., Su, W., Nguyen, C., Corbett, J.G., Liang, L., Mitrescu, C., Rose, F.G., Kato, S., 2018. Clouds and the earth's radiant energy system (CERES) energy balanced and filled (EBAF) top-of-atmosphere (TOA) edition-4.0 data product. J. Clim. 31 (2), 895–918. http://dx.doi.org/10.1175/jcli-d-17-0208.1.

Loeb, N.G., Thorsen, T.J., Kato, S., Rose, F.G., Hodnebrog, O., Myhre, G., 2025. Emerging hemispheric asymmetry of Earth's radiation. Proc. Natl. Acad. Sci. 122 (40), http://dx.doi.org/10.1073/pnas.2511595122.

Loew, A., Andersson, A., Trentmann, J., Schröder, M., 2016. Assessing surface solar radiation fluxes in the CMIP ensembles. J. Clim. 29 (20), 7231–7246. http://dx.doi.org/10.1175/jcli-d-14-00503.1.

Lohmann, U., Feichter, J., 2005. Global indirect aerosol effects: a review. Atmospheric Chem. Phys. 5 (3), 715–737. http://dx.doi.org/10.5194/acp-5-715-2005.

Lu, X., Mao, F., Rosenfeld, D., Zhu, Y., Zang, L., Pan, Z., Gong, W., 2023. The temperature control of cloud adiabatic fraction and coverage. Geophys. Res. Lett. 50 (22), http://dx.doi.org/10.1029/2023gl105831.

Luo, H., Quaas, J., Han, Y., 2024. Diurnally asymmetric cloud cover trends amplify greenhouse warming. Sci. Adv. 10 (25), http://dx.doi.org/10.1126/sciadv.ado5179.

Mateos, D., Sanchez-Lorenzo, A., Antón, M., Cachorro, V., Calbó, J., Costa, M.J., Torres, B., Wild, M., 2014. Quantifying the respective roles of aerosols and clouds in the strong brightening since the early 2000s over the Iberian Peninsula. J. Geophys. Res.: Atmospheres 119 (17), 10–382. http://dx.doi.org/10.1002/2014JD022076.

McCoy, D.T., Eastman, R., Hartmann, D.L., Wood, R., 2017. The change in low cloud cover in a warmed climate inferred from AIRS, MODIS, and ERA-interim. J. Clim. 30 (10), 3609–3620. http://dx.doi.org/10.1175/jcli-d-15-0734.1.

Mendoza, V., Pazos, M., Garduño, R., Mendoza, B., 2021. Thermodynamics of climate change between cloud cover, atmospheric temperature and humidity. Sci. Rep. 11 (1), http://dx.doi.org/10.1038/s41598-021-00555-5.

Modak, A., Mauritsen, T., 2021. The 2000–2012 global warming hiatus more likely with a low climate sensitivity. Geophys. Res. Lett. 48 (9), http://dx.doi.org/10.1029/2020gl091779.

Müller, J., Folini, D., Wild, M., Pfenninger, S., 2019. CMIP-5 models project photovoltaics are a no-regrets investment in Europe irrespective of climate change. Energy 171, 135–148. http://dx.doi.org/10.1016/j.energy.2018.12.139.

Müller, R., Pfeifroth, U., 2022. Remote sensing of solar surface radiation–a reflection of concepts, applications and input data based on experience with the effective cloud albedo. Atmospheric Meas. Tech. 15 (5), 1537–1561. http://dx.doi.org/10.5194/amt-15-1537-2022.

NOAA NCEI, 2025a. Climate at a glance: Global time series. https://www.ncei.noaa.gov/access/monitoring/climate-at-a-glance/global/time-series. (Accessed 12 June 2025).

NOAA NCEI, 2025b. Climate forecast system reanalysis (CFSR), for 1979 to 2011. https://www.ncei.noaa.gov/access/metadata/landing-page/bin/iso?id=gov.noaa.ncdc:C00765. (Accessed 24 April 2025).

NOAA NCEI, 2025c. Global forecast system (GFS). https://www.ncei.noaa.gov/products/weather-climate-models/global-forecast. (Accessed 24 April 2025).

Ohmura, A., 2009. Observed decadal variations in surface solar radiation and their causes. J. Geophys. Res.: Atmospheres 114 (D10), http://dx.doi.org/10.1029/2008JD011290.

O'Neill, B.C., Tebaldi, C., van Vuuren, D.P., Eyring, V., Friedlingstein, P., Hurtt, G., Knutti, R., Kriegler, E., Lamarque, J.-F., Lowe, J., Meehl, G.A., Moss, R., Riahi, K., Sanderson, B.M., 2016. The scenario model intercomparison project (ScenarioMIP) for CMIP6. Geosci. Model. Dev. 9 (9), 3461–3482. http://dx.doi.org/10.5194/gmd-9-3461-2016.

Padma Kumari, B., Goswami, B.N., 2010. Seminal role of clouds on solar dimming over the Indian monsoon region. Geophys. Res. Lett. 37 (6), http://dx.doi.org/10.1029/2009GL042133.

Perez, R., Cebecauer, T., Šúri, M., 2013. Semi-empirical satellite models. In: Kleissl, J. (Ed.), Solar Energy Forecasting and Resource Assessment. Academic Press, Boston, pp. 21–48. http://dx.doi.org/10.1016/B978-0-12-397177-7.00002-4.

Petrie, R., Denvil, S., Ames, S., Levavasseur, G., Fiore, S., Allen, C., Antonio, F., Berger, K., Bretonnière, P.-A., Cinquini, L., Dart, E., Dwarakanath, P., Druken, K., Evans, B., Franchistéguy, L., Gardoll, S., Gerbier, E., Greenslade, M., Hassell, D., Iwi, A., Juckes, M., Kindermann, S., Lacinski, L., Mirto, M., Nasser, A.B., Nassisi, P., Nienhouse, E., Nikonov, S., Nuzzo, A., Richards, C., Ridzwan, S., Rixen, M., Serradell, K., Snow, K., Stephens, A., Stockhause, M., Vahlenkamp, H., Wagner, R., 2021. Coordinating an operational data distribution network for CMIP6 data. Geosci. Model. Dev. 14 (1), 629–644. http://dx.doi.org/10.5194/gmd-14-629-2021.

Pettitt, A.N., 1979. A non-parametric approach to the change-point problem. Appl. Opt. 28 (2), 126. http://dx.doi.org/10.2307/2346729.

Petty, G.W., 2006. A First Course in Atmospheric Radiation, second ed. Sundog Publishing.

Pfeifroth, U., Drücke, J., Kothe, S., Trentmann, J., Schröder, M., Hollmann, R., 2024. SARAH-3 – satellite-based climate data records of surface solar radiation. Earth Syst. Sci. Data 16 (11), 5243–5265. http://dx.doi.org/10.5194/essd-16-5243-2024, URL: https://essd.copernicus.org/articles/16/5243/2024/.

Pfeifroth, U., Sanchez-Lorenzo, A., Manara, V., Trentmann, J., Hollmann, R., 2018. Trends and variability of surface solar radiation in Europe based on surface-and satellite-based data records. J. Geophys. Res.: Atmospheres 123 (3), 1735–1754. http://dx.doi.org/10.1002/2017JD027418.

Pinker, R., Zhang, B., Dutton, E., 2005. Do satellites detect trends in surface solar radiation? Sci. 308 (5723), 850–854. http://dx.doi.org/10.1126/science.1103159.

Pöhlker, M.L., Pöhlker, C., Quaas, J., Mülmenstädt, J., Pozzer, A., Andreae, M.O., Artaxo, P., Block, K., Coe, H., Ervens, B., et al., 2023. Global organic and inorganic aerosol hygroscopicity and its effect on radiative forcing. Nat. Commun. 14 (1), 6139.

Randles, C.A., da Silva, A.M., Buchard, V., Colarco, P.R., Darmenov, A., Govindaraju, R., Smirnov, A., Holben, B., Ferrare, R., Hair, J., Shinozuka, Y., Flynn, C.J., 2017. The MERRA-2 aerosol reanalysis, 1980 onward. Part I: System description and data assimilation evaluation. J. Clim. 30 (17), 6823–6850. http://dx.doi.org/10.1175/jcli-d-16-0609.1.

Riahi, K., van Vuuren, D.P., Kriegler, E., Edmonds, J., O'Neill, B.C., Fujimori, S., Bauer, N., Calvin, K., Dellink, R., Fricko, O., Lutz, W., Popp, A., Cuaresma, J.C., KC, S., Leimbach, M., Jiang, L., Kram, T., Rao, S., Emmerling, J., Ebi, K., Hasegawa, T., Havlik, P., Humpenöder, F., Da Silva, L.A., Smith, S., Stehfest, E., Bosetti, V., Eom, J., Gernaat, D., Masui, T., Rogelj, J., Strefler, J., Drouet, L., Krey, V., Luderer, G., Harmsen, M., Takahashi, K., Baumstark, L., Doelman, J.C., Kainuma, M., Klimont, Z., Marangoni, G., Lotze-Campen, H., Obersteiner, M., Tabeau, A., Tavoni, M., 2017. The Shared Socioeconomic Pathways and their energy, land use, and greenhouse gas emissions implications: An overview. Glob. Environ. Chang. 42, 153–168. http://dx.doi.org/10.1016/j.gloenvcha.2016.05.009.

Rosenfeld, D., Sherwood, S., Wood, R., Donner, L., 2014. Climate effects of aerosol-cloud interactions. Sci. 343 (6169), 379–380. http://dx.doi.org/10.1126/science.1247490.

Ruiz-Arias, J.A., 2023. SPARTA: Solar parameterization for the radiative transfer of the cloudless atmosphere. Renew. Sustain. Energy Rev. 188, 113833. http://dx.doi.org/10.1016/j.rser.2023.113833.

Ruiz-Arias, J.A., Arbizu-Barrena, C., Santos-Alamillos, F.J., Tovar-Pescador, J., Pozo-Vázquez, D., 2016. Assessing the surface solar radiation budget in the WRF model: A spatiotemporal analysis of the bias and its causes. Mon. Weather Rev. 144 (2), 703–711. http://dx.doi.org/10.1175/mwr-d-15-0262.1.

Ruiz-Arias, J.A., Cebecauer, T., Tovar-Pescador, J., Šúri, M., 2010. Spatial disaggregation of satellite-derived irradiance using a high-resolution digital elevation model. Sol. Energy 84 (9), 1644–1657. http://dx.doi.org/10.1016/j.solener.2010.06.002.

Rutan, D.A., Kato, S., Doelling, D.R., Rose, F.G., Nguyen, L.T., Caldwell, T.E., Loeb, N.G., 2015. CERES synoptic product: Methodology and validation of surface radiant flux. J. Atmos. Ocean. Technol. 32 (6), 1121–1143. http://dx.doi.org/10.1175/jtech-d-14-00165.1.

Sanchez-Lorenzo, A., Enriquez-Alonso, A., Wild, M., Trentmann, J., Vicente-Serrano, S.M., Sanchez-Romero, A., Posselt, R., Hakuba, M.Z., 2017. Trends in downward surface solar radiation from satellites and ground observations over Europe during 1983–2010. Remote Sens. Environ. 189, 108–117. http://dx.doi.org/10.1016/j.rse.2016.11.018.

Sanchez-Lorenzo, A., Wild, M., Brunetti, M., Guijarro, J.A., Hakuba, M.Z., Calbó, J., Mystakidis, S., Bartok, B., 2015. Reassessment and update of long-term trends in downward surface shortwave radiation over Europe (1939–2012). J. Geophys. Res.: Atmospheres 120 (18), 9555–9569. http://dx.doi.org/10.1002/2015jd023321.

Sanchez-Lorenzo, A., Wild, M., Trentmann, J., 2013. Validation and stability assessment of the monthly mean CM SAF surface solar radiation dataset over Europe against a homogenized surface dataset (1983–2005). Remote Sens. Environ. 134, 355–366. http://dx.doi.org/10.1016/j.rse.2013.03.012.

Schilliger, L., Tetzlaff, A., Bourgeois, Q., Correa, L.F., Wild, M., 2024. An investigation on causes of the detected surface solar radiation brightening in Europe using satellite data. J. Geophys. Res.: Atmospheres 129 (15), http://dx.doi.org/10.1029/2024jd041101.

Schneider, T., Kaul, C.M., Pressel, K.G., 2019. Possible climate transitions from breakup of stratocumulus decks under greenhouse warming. Nat. Geosci. 12 (3), 163–167. http://dx.doi.org/10.1038/s41561-019-0310-1.

Solargis, 2025. Solargis web site. https://solargis.com. (Accessed 4 May 2025).

Šúri, M., Cebecauer, T., 2014. Satellite-based solar resource data: Model validation statistics versus user's uncertainty. In: ASES SOLAR 2014 Conference, San Francisco. pp. 7–9.

Tobin, I., Greuell, W., Jerez, S., Ludwig, F., Vautard, R., van Vliet, M.T.H., Bréon, F.-M., 2018. Vulnerabilities and resilience of European power generation to 1.5 °C, 2 °C and 3 °C warming. Environ. Res. Lett. 13 (4), 044024. http://dx.doi.org/10.1088/1748-9326/aab211.

Turnock, S., Spracklen, D., Carslaw, K., Mann, G., Woodhouse, M., Forster, P., Haywood, J., Johnson, C., Dalvi, M., Bellouin, N., et al., 2015. Modelled and observed changes in aerosols and surface solar radiation over Europe between 1960 and 2009. Atmospheric Chem. Phys. 15 (16), 9477–9500. http://dx.doi.org/10.5194/acp-15-9477-2015.

Twomey, S., 1977. The influence of pollution on the shortwave albedo of clouds. J. Atmos. Sci. 34 (7), 1149–1152. http://dx.doi.org/10.1175/1520-0469(1977)034<1149:tiopot>2.0.co;2.

Urraca, R., Trentmann, J., Pfeifroth, U., Gobron, N., 2024. Can satellite products monitor solar brightening in Europe? Remote Sens. Environ. 315, 114472. http://dx.doi.org/10.1016/j.rse.2024.114472.

Vose, R.S., Huang, B., Yin, X., Arndt, D., Easterling, D.R., Lawrimore, J.H., Menne, M.J., Sanchez-Lugo, A., Zhang, H.M., 2021. Implementing full spatial coverage in NOAA's global temperature analysis. Geophys. Res. Lett. 48 (4), http://dx.doi.org/10.1029/2020gl090873.

Wild, M., 2009. Global dimming and brightening: A review. J. Geophys. Res.: Atmospheres 114 (D10), http://dx.doi.org/10.1029/2008JD011470.

Wild, M., 2012. Enlightening global dimming and brightening. Bull. Am. Meteorol. Soc. 93 (1), 27–37. http://dx.doi.org/10.1175/BAMS-D-11-00074.1.

Wild, M., Folini, D., Henschel, F., Fischer, N., Müller, B., 2015. Projections of long-term changes in solar radiation based on CMIP5 climate models and their influence on energy yields of photovoltaic systems. Sol. Energy 116, 12–24. http://dx.doi.org/10.1016/j.solener.2015.03.039.

Wild, M., Folini, D., Schär, C., Loeb, N., Dutton, E.G., König-Langlo, G., 2013. The global energy balance from a surface perspective. Clim. Dyn. 40 (11), 3107–3134. http://dx.doi.org/10.1007/s00382-012-1569-8.

Wild, M., Gilgen, H., Roesch, A., Ohmura, A., Long, C.N., Dutton, E.G., Forgan, B., Kallis, A., Russak, V., Tsvetkov, A., 2005. From dimming to brightening: Decadal changes in solar radiation at Earth's surface. Sci. 308 (5723), 847–850. http://dx.doi.org/10.1126/science.1103215.

Wild, M., Ohmura, A., Schär, C., Müller, G., Folini, D., Schwarz, M., Hakuba, M.Z., Sanchez-Lorenzo, A., 2017. The Global Energy Balance Archive (GEBA) version 2017: A database for worldwide measured surface energy fluxes. Earth Syst. Sci. Data 9 (2), 601–613. http://dx.doi.org/10.5194/essd-9-601-2017.

World Bank Group, 2019. Global Solar Radiation Atlas 2.0: Validation Report. Technical Report 149878, Energy Sector Management Assistance Program, Washington, D.C., URL: http://documents.worldbank.org/curated/en/507341592893487792/Global-Solar-Atlas-2-0-Validation-Report.

Yan, X.-H., Boyer, T., Trenberth, K., Karl, T.R., Xie, S.-P., Nieves, V., Tung, K.-K., Roemmich, D., 2016. The global warming hiatus: Slowdown or redistribution? Earth's Future 4 (11), 472–482. http://dx.doi.org/10.1002/2016ef000417.

Yuan, T., Song, H., Wood, R., Oreopoulos, L., Platnick, S., Wang, C., Yu, H., Meyer, K., Wilcox, E., 2023b. Observational evidence of strong forcing from aerosol effect on low cloud coverage. Sci. Adv. 9 (45), http://dx.doi.org/10.1126/sciadv.adh7716.

Yuan, P., Van Malderen, R., Yin, X., Vogelmann, H., Jiang, W., Awange, J., Heck, B., Kutterer, H., 2023a. Characterisations of Europe's integrated water vapour and assessments of atmospheric reanalyses using more than 2 decades of ground-based GPS. Atmospheric Chem. Phys. 23 (6), 3517–3541. http://dx.doi.org/10.5194/acp-23-3517-2023.

Zhang, C., Li, S., Luo, F., Huang, Z., 2019. The global warming hiatus has faded away: An analysis of 2014–2016 global surface air temperatures. Int. J. Climatol. 39 (12), 4853–4868. http://dx.doi.org/10.1002/joc.6114.